J. Fluid Mech. (2014), *vol.* 743, *pp.* 202–248.
doi:10.1017/jfm.2013.629

Large-scale contribution to mean wall shear stress in high-Reynolds-number flat-plate boundary layers up to Re_θ=13 650

Sébastien Deck†, Nicolas Renard, Romain Laraufie and Pierre-Élie Weiss

ONERA, The French Aerospace Lab, F-92190 Meudon, France

(Received 9 July 2013; revised 7 November 2013; accepted 26 November 2013;
first published online 4 March 2014)

A numerical investigation of the mean wall shear stress properties on a spatially developing turbulent boundary layer over a smooth flat plate was carried out by means of a zonal detached eddy simulation (ZDES) technique for the Reynolds number range $3060 \leqslant Re_\theta \leqslant 13\,650$. Some asymptotic trends of global parameters are suggested. Consistently with previous findings, the calculation confirms the occurrence of very large-scale motions approximately 5δ to 6δ long which are meandering with a lateral amplitude of 0.3δ and which maintain a footprint in the near-wall region. It is shown that these large scales carry a significant amount of Reynolds shear stress and their influence on the skin friction, denoted $C_{f,2}$, is revisited through the FIK identity by Fukagata, Iwamoto & Kasagi (*Phys. Fluids*, vol. 14, 2002, p. L73). It is argued that $C_{f,2}$ is the relevant parameter to characterize the high-Reynolds-number turbulent skin friction since the term describing the spatial heterogeneity of the boundary layer also characterizes the total shear stress variations across the boundary layer. The behaviour of the latter term seems to follow some remarkable self-similarity trends towards high Reynolds numbers. A spectral analysis of the weighted Reynolds stress with respect to the distance to the wall and to the wavelength is provided for the first time to our knowledge and allows us to analyse the influence of the largest scales on the skin friction. It is shown that structures with a streamwise wavelength $\lambda_x > \delta$ contribute to more than 60 % of $C_{f,2}$, and that those larger than $\lambda_x > 2\delta$ still represent approximately 45 % of $C_{f,2}$.

Key words: boundary layer structure, turbulent boundary layer, turbulence simulation

1. Introduction

Mean wall shear stress plays a key role in many phenomena. In engineering applications, accurate assessment of the skin friction coefficient is required for determining friction drag on a body moving relative to a fluid. This enables performance prediction (e.g. fuel consumption). A better understanding of mean friction generation could even help to design new friction reduction devices. Mean friction over a smooth surface can also play a key role in some geophysical flows such as the atmospheric surface layer (Hutchins *et al.* 2012), wind-driven surface

† Email address for correspondence: sebastien.deck@onera.fr

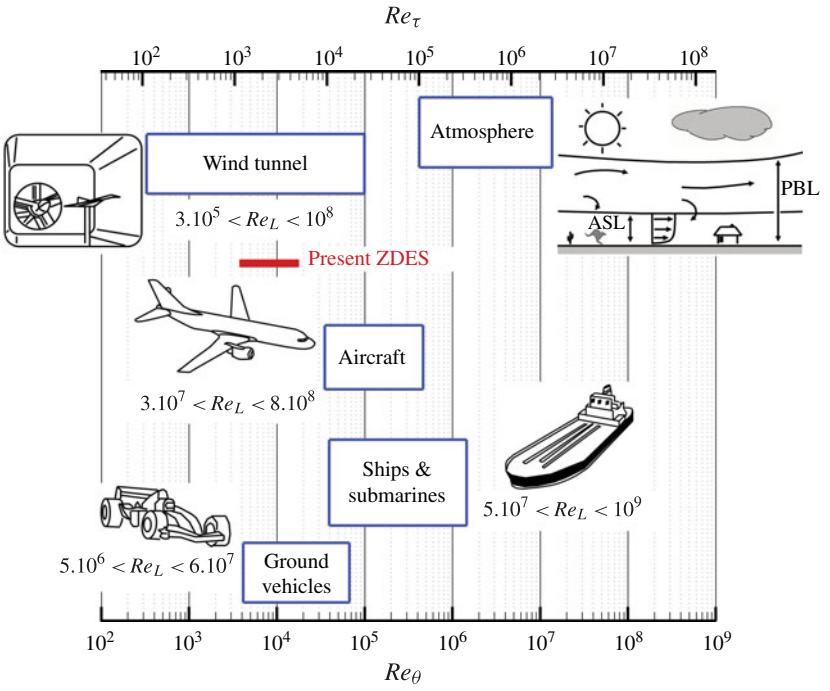

FIGURE 1. (Colour online) Typical Reynolds numbers in boundary layer applications. Re_L and Re_θ denote the Reynolds numbers based on the streamwise characteristic length and momentum thickness respectively. Re_τ denotes the friction Reynolds number. The relation $Re_\tau = f(Re_\theta)$ is the one proposed in (3.1). ASL: atmospheric surface sayer; PBL: planetary boundary layer.

currents in the ocean or wave dissipation by bottom friction. Given the large scales involved, these flows are most often characterized by a high Reynolds number and a fully developed turbulence (see figure 1). Though it is widely acknowledged that both high-quality experiments and numerical simulations are essential to understand the kinematics and dynamics of the coherent structures populating the turbulent boundary layer, surprisingly little attention in the literature has been devoted to the understanding of mean skin friction generation in a boundary layer.

Since mean wall shear stress is directly related to the normal gradient of mean streamwise velocity at the wall, itself resulting from the turbulent mixing of streamwise momentum, the inner region of the boundary layer seems to be of highest interest regarding mean friction generation. Its dynamics has been extensively studied at rather low Reynolds numbers, typically $Re_\theta \leqslant 5000$, for practical reasons. This led to the characterization of the coherent structures populating the inner layer at low Reynolds numbers, which scale in wall units and consist of quasi-streamwise vortices and low- and high-speed near-wall streaks, as well as of several kinds of hairpin-like structures. A thorough review of these structures can be found in Robinson (1991). The dynamics of near-wall structures was shown to be self-sustaining, at least at low Reynolds numbers. Several possible explanations on how coherent structures can regenerate each other in a closed cycle are described in Jiménez & Pinelli (1999) and in Panton (2001). This suggests that mean wall shear stress could result only from near-wall dynamics, possibly independent of the outer layer. It follows from this

hypothesis that reducing mean friction at low Reynolds numbers could be achieved by means of controlling the near-wall dynamics using local devices such as ribblets. However, mean friction in a turbulent boundary layer depends dramatically on the external flow, the most extreme example of which being the boundary layer separation occurring in the presence of a strong enough adverse pressure gradient. This shows that the possibly universal inner layer behaviour must be at least modulated by some events scaling in outer units and originating from the outer part of the boundary layer. At moderate Reynolds numbers, the outer length scale (i.e. the boundary layer thickness) tends to be much larger than the wall unit, which implies that the influence of these outer events on mean friction can be traced back to the contribution of large-scale events to friction.

The outer region of the boundary layer is populated with many coherent structures, described in Robinson (1991) at moderate Reynolds numbers. Experimental visualization of some of the largest of these structures can be found in Head & Bandyopadhyay (1981) up to high Reynolds numbers (Re_θ up to 17 350), whereas particle image velocimetry (PIV) data are available up to moderately high Reynolds numbers, such as the example presented in Carlier & Stanislas (2005). The attached-eddy hypothesis first presented in Townsend (1976) suggests that some of these structures should be hairpin-like structures extending down to the wall, hence called attached eddies. However, unattached structures seem to exist as well, as suggested by models such as in Perry & Marusic (1995) where it was shown that it is not possible to predict the actual velocity and turbulence intensity profiles in the boundary layer by means of solely the attached eddies. Evidence shown in Adrian, Meinhart & Tomkins (2000) suggests that small structures tend to cluster in packets. This preferential spatial distribution results in bursting events, large-scale shear layers and zones of approximately uniform streamwise velocity. As a consequence, the interpretation of large-scale structures revealed for example by spectral analysis is not straightforward. Referring to a large-scale structure does not necessarily imply a single entity of large scale. It can consist of a cluster of spatially coherent structures, which themselves tend to be made of small structures cascading towards dissipative and quasi-isotropic scales. The decomposition into smaller scales at higher Reynolds numbers is emphasized in Jiménez (2012). The difficulty in the interpretation of spectral results in the presence of clusters of structures that are not straight but meandering is detailed in Smits, McKeon & Marusic (2011), Jiménez, del Álamo & Flores (2004), Hutchins & Marusic (2007).

At low to moderate Reynolds numbers, the lack of scale separation between inner and outer scalings leads to some confusion between inner and outer layer events. On the other hand, at higher Reynolds numbers, i.e. $Re_\theta \geqslant 10\,000$, the scale separation becomes clearer. Many experimental results and a few direct numerical simulations have suggested that the trend towards high Reynolds numbers could reveal some fundamentally different mechanisms at work in the dynamics of a high-Reynolds-number boundary layer compared to its lower-Reynolds-number counterpart. It is not clear whether the phenomena observed at high Reynolds numbers are missing at lower Reynolds numbers or simply cannot be observed because they are mixed with other phenomena due to the lack of scale separation. Moreover, performing a reliable experiment or simulation becomes increasingly difficult at higher Reynolds numbers. A thorough summary of the experimental issues that have jeopardized the reliability of some of the high-Reynolds-number results is given in Marusic *et al.* (2010). Most of the observed trends towards higher Reynolds numbers are still raising open questions on their reliability and, if they can be trusted, on

their physical explanation. Two contrasted reviews of the main issues can be found in Jiménez (2012) and in Smits *et al.* (2011), a short summary of which is given in the following. A thorough description of the main issues related to turbulent boundary layers may be found in Klewicki (2010).

One first observation for increasing Reynolds numbers is that the streamwise velocity fluctuations intensity, which peaks at 15 wall units from the wall at low Reynolds numbers, seems to present an increase in its maximum value when scaled with inner quantities (i.e. wall unit and friction velocity), together with the growth of an outer plateau which could even result in an outer peak located near the geometric centre of the logarithmic layer located around $y^+ = 3.9\,Re_\tau^{1/2}$ (see Marusic, Mathis & Hutchins 2010*a*). The appearance of the outer peak, which could also be present in the turbulent kinetic energy production term, is put into question in Jiménez (2012) because of the experimental issues caused by the difficulty of performing reliable measurements at high Reynolds numbers. However, the fact that the inner peak does not scale in inner units is predicted by the attached-eddy hypothesis (see Townsend 1976; Perry & Marusic 1995), and other scalings have been successfully considered, for instance in DeGraaff & Eaton (2000). Spectral analysis performed in Hutchins & Marusic (2007) suggests that the outer peak could be caused by large-scale structures located in the outer layer, while the increase of the inner peak could result from the imprint of the outer large-scale structures, the foot of which is superimposed onto the smaller inner structures in agreement with the attached-eddy theory. This reasoning is backed up by a scale decomposition of the streamwise fluctuating velocity intensity across the boundary layer, presented in Smits *et al.* (2011) and suggesting that large scales tend to be increasingly important at higher Reynolds numbers.

These increasingly large structures could be up to 15 boundary layer thicknesses long, and their visualization suggests they have a meandering shape, possibly resulting from instabilities in their early stages. They are called very large-scale motions (VLSM) or superstructures. It should be emphasized that these structures seem to be different in a flat-plate boundary layer, which is the topic of the present study, from what they may be in a channel or a pipe flow, as described by Jiménez (1998) and confirmed in Balakumar & Adrian (2007). Further differences between the flat-plate boundary layer and other wall-bounded flows are given in Marusic *et al.* (2010). Because of the numerous applications that have been evoked, the present study focuses on the flat-plate boundary layer rather than on internal wall-bounded flows.

Another trend that has been reported is the increasing modulation of the inner layer activity by the outer layer. In addition to the superposition of large scales originating in the outer layer onto the inner layer, the intensity of the dynamics of the inner layer seems to be directly modulated by the large-scale events passing by in the above outer layer, as described and discussed in Mathis, Hutchins & Marusic (2009), Marusic, Mathis & Hutchins (2010*b*), Schlatter & Örlü (2010*b*), Bernardini & Pirozzoli (2011), Mathis *et al.* (2011), Jiménez (2012), Ganapathisubramani *et al.* (2012).

One major question concerning the large-scale structures is whether they are active or inactive in the sense of Townsend (1976), i.e. whether or not they contribute to the Reynolds shear stress, to which the mean friction is directly related. In the framework of the attached-eddy hypothesis, it seems likely that a given structure is active at a height of the same order as its size, but is inactive near the wall, where the normal velocity it induces is limited by the no-penetration constraint at the wall. This could suggest that the largest scales, for instance those with a streamwise wavelength larger than the boundary layer thickness, do not contribute much to the mean friction. However, there has been some experimental and numerical

evidence that the large scales contribute much to the Reynolds shear stress, and may represent a non-negligible part of the turbulent contribution to mean friction. Some insight into this question in the channel and pipe flow cases may be found in many references such as del Álamo *et al.* (2004), Jiménez *et al.* (2004) or Hoyas & Jimenez (2006). In the case that is considered in the present study, i.e. the flat-plate turbulent boundary layer, much less information can be found in the literature. Evaluations of the contribution of the large-scale structures to the Reynolds shear stress can be found in Ganapathisubramani, Longmire & Marusic (2003) and in Marusic & Hutchins (2005) at some wall-normal locations. Co-spectra of the Reynolds shear stresses are shown in several experimental data sets, such as Marusic, Li & Perry (1989), Krogstad, Antonia & Browne (1992), Saddoughi & Veeravalli (1994), Nickels & Marusic (2001), Kunkel & Marusic (2006) and Balakumar & Adrian (2007). Even more refined signal processing tools have been used, such as wavelet transforms in Hudgins, Friehe & Mayer (1993), and a complete study was devoted to the motions contributing to the Reynolds shear stress in Priyadarshana & Klewicki (2004). Unfortunately, insufficient data were gathered to cover the contribution of the large scales to the Reynolds shear stress across the whole boundary layer thickness, which would be very useful to determine to what extent they contribute to mean wall shear stress. The available data do not fully represent the evolution with the Reynolds number of the contribution of large scales to the Reynolds shear stress either. As emphasized by Balakumar & Adrian (2007), even though it has been shown that the large scales carry a non-negligible amount of Reynolds shear stress, a comprehensive analysis of their contribution to mean friction depending also on the Reynolds number is not yet available. Very recently, Hwang (2013) presented a study of the Reynolds number trend in the case of a channel flow at relatively low Reynolds numbers, revealing that the relative contribution to mean skin friction by larger-scale structures increases significantly with the Reynolds number. Such a study in the higher-Reynolds-number flat-plate turbulent boundary layer case is still missing. The direct contribution to mean skin friction of the structures located in the outer layer has not yet been made clear either.

One of the reasons for this lack of data is the challenge that computing a high-Reynolds-number boundary layer represents. In contrast to the well-characterized high-Reynolds-number isotropic turbulence (Kaneda & Ishihara 2006; Ishihara, Gotoh & Kaneda 2009), the simulation of wall turbulence at high Reynolds numbers is still a serious challenge (see the discussion by Sagaut & Deck 2009). Indeed, in the framework of isotropic flows, classical theory tells us that energy production and dissipation peaks are independent of each other, and that they only interact through the intermediate inertial cascade, which is universal. A major difference with wall-bounded flows is that the dissipative structures in the lower buffer region are also responsible for a large fraction of the turbulent energy production, and have a major influence on, among other things, the overall friction coefficient. In addition, Jiménez (2003) emphasized that for the same scale separation, wall-bounded simulations are more expensive than isotropic ones, both because the inhomogeneity of the flow results in slightly larger grid requirements, and because the presence of a mean flow velocity requires shorter time steps. The majority of published studies concerns the fully developed channel flows instead of a spatially developing boundary layer over a smooth flat plate, for several reasons. First is the difficulty of prescribing correct inflow conditions since, conversely to the channel flow configuration, the unsteady character of the flow field is not imposed by a forcing term in the movement associated with periodic boundary conditions. Secondly, the streamwise inhomogeneity

of the flat-plate boundary layer is harder to compute and increases the computational resources required to simulate this spatially developing wall-bounded flow.

Smits *et al.* (2011) emphasized that pipe, channel, and boundary layer flows may behave differently in various aspects and in particular Marusic *et al.* (2010) reviewed the significant differences between channel and boundary layer flows even in the inner regions. Similarly, Lee & Sung (2013) used direct numerical simulations (DNS) to investigate the similarities and differences of very large-scale motions between a flat-plate turbulent boundary layer and a fully developed turbulent pipe flow. They found that the average streamwise length scale of the pipe flow was up to three times larger through the log and wake regions than that of a flat-plate boundary layer. Thus from now on, only flat-plate boundary layer flows will be considered. For instance, table 1 summarizes some numerical studies concerning only the spatially developing flat-plate turbulent boundary layers. Only numerical studies which are compared with experimental (or DNS) results are considered. Apart from different numerical discretization schemes and resolutions, the simulations outlined in table 1 exhibit very significant differences in domain length, unsteady boundary conditions and inlet Reynolds numbers. Recent examples of incompressible boundary layers (Schlatter & Örlü 2010*a*; Sillero *et al.* 2011) reach friction Reynolds numbers $Re_\tau \approx 2000$. Pirozzoli & Bernardini (2013) proposed a DNS at $Re_\tau \approx 4000$ in the low supersonic regime in the restricted Reynolds number range $13\,320 \leqslant Re_\theta \leqslant 15\,489$. These DNS are comparable to the largest DNS of channel flow currently available (Hoyas & Jimenez 2006; Kaneda, Morishita & Ishihara 2013). As reminded earlier, very little is known about the mean skin friction generation at these high Reynolds numbers and in this paper we investigate numerically for the first time to the authors' knowledge this problem for a wide Reynolds number range $3500 \leqslant Re_\theta \leqslant 13\,650$.

On the theoretical side, Fukagata, Iwamoto & Kasagi (2002) derived an analytical expression (referred to as the FIK identity in the following) relating the local skin friction coefficient to the properties of the flow above the surface for canonical cases of turbulent plane channel flow, pipe flow, and flat-plate boundary layers. These authors have shown that the skin friction coefficient depends on a weighted integral of the Reynolds shear stress distribution. Extensions of this theory that may be found in the literature will be further discussed in the section devoted to the FIK identity. However, surprisingly little use of the FIK identity has been made in the case of the flat-plate boundary layer so far, in comparison with the numerous and successful analysis made using this identity in the case of internal wall-bounded flows. The present study proposes some new insight into how the FIK identity may be used in a high-Reynolds-number flat-plate boundary layer to assess the large-scale contribution to mean wall shear stress.

This short review reveals that the detailed knowledge of the large-scale contribution to mean wall shear stress at high Reynold numbers is severely limited by the lack of experimental data and advanced numerical simulations. This is exactly the scope of this article, which is organized as follows. In § 2 the simulation methodology is presented as well as the test case. Both Reynolds-averaged and spectral data are compared with the available experimental data and those found in the literature in § 3. The decomposition of the turbulent mean friction coefficient into several physical sources through the FIK identity is investigated in § 4. In § 5, the scale decomposition of mean wall shear stress is investigated with the help of spectral analysis.

https://doi.org/10.1017/jfm.2013.629 Published online by Cambridge University Press

Reference	Model	Inflow fluctuation	δ_0^+	Re_θ	Δx	Δy	Δz	$N_{xyz} \times 10^6$
Spalart (1988)	DNS (S)	RECY	–	225–1410	20^+	–	6.7^+	11
Simens *et al.* (2009)	DNS (FD/S)	RECY	–	620–2140	6.1^+	0.3^+	4^+	3398
Schlatter & Örlü (2010*a*)	DNS(S)	TR at $Re_\theta = 180$	45	180–4300	9^+	–	4^+	3227
Wu & Moin (2009)	DNS (FD)	FP	–	80–940	5.9^+	–	11^+	209
Araya *et al.* (2011)	DNS (FE)	RECY	980	2667–3005	20^+	0.5^+	10^+	7.5
Ferrante & Elghobashi (2009)	DNS (FD)	RECY	–	2340–2900	$L_x = 10\delta_0$ 7.25^+ to 15.8^+	$L_y = 3\delta_0$ 0.58^+ to 1.26^+	$L_z = 1.6\delta_0$ 3.6^+ to 7.9^+	67
Sillero *et al.* (2011)	DNS(FD/S)	PC	–	2780–6650	$L_x = 20\delta_0$ 7^+	$L_y = 5\delta_0$ 0.32^+	$L_z = 7\delta_0$ 4.07^+	33 660
Lee & Sung (2011)	DNS(FD)	RECY	270	1410–2560	12.3^+	0.06^+	4.9^+	315
Lee *et al.* (2013)	DNS(FD)	PC	–	1240–2060	$L_x = 33\delta_0$ 5.08^+	$L_y = 3.3\delta_0$ 0.246^+	$L_z = 3.3\delta_0$ 3.25^+	2021
Pirozzoli & Bernardini (2013)	DNS (FD)	RECY	843	2827–3878	6.5^+	0.7^+	5.6^+	2030
	DNS (FD)	RECY	3413	13 320–15 489	$L_x = 100\delta_0$ 6.5^+	– 0.9^+	$L_z = 9\delta_0$ 5.5^+	34 000
Schlatter *et al.* (2010)	LES(S)	TR at $Re_\theta = 180$	45	180–4300	$L_x = 70\delta_0$ 25.3^+	–	$L_z = 6.2\delta_0$ 10.8^+	606
Tromeur, Garnier & Sagaut (2006)	LES (FV)	RECY	–	2917	50^+	0.5^+	18^+	2.0
Pamiès *et al.* (2009)	LES (FV)	RECY and ST	1100	3535	44^+	1^+	14^+	–
Deck *et al.* (2011)	ZDES and LES (FV)	RECY and ST	750	1750–2900	$L_x = 7.5\delta_0$ 50^+	$L_y = 4\delta_0$ 1^+	$L_z = 2\delta_0$ 12^+	15
Present	ZDES (FV)	ST	1070	3060–13 650	$L_x = 120\delta_0$ 50^+ $L_x = 342\delta_0$	$L_y = 10\delta_0$ 1^+ $L_y = 41\delta_0$	$L_z = 4\delta_0$ 12^+ $L_z = 8.6\delta_0$	806

TABLE 1. Example of spatially developing boundary layer simulations. Re_θ and $\delta_0^+ = Re_\tau$ are the Reynolds numbers based respectively on the momentum thickness and the friction velocity at the inlet. L_x, L_y and L_z denote respectively the size of the computational domain in the streamwise, wall-normal and spanwise directions normalized by the initial boundary layer thickness δ_0. The Δ^+ are the corresponding resolutions expressed in wall units. N_{xyz} refers to the number of grid points. RECY, PC and ST refer to respectively the recycling, the precursor calculation and synthetic turbulence methods used to generate inflow fluctuations while TR and FP mean respectively that the incoming laminar boundary layer has been tripped and that free-stream turbulence has been imposed. FV, FD, FE, S refer to the numerical method, respectively finite-volume, finite-difference, finite-element and spectral method.

2. Simulation overview

2.1. *General description*

The FLU3M code developed by ONERA is used to solve the compressible Navier–Stokes equations on multiblock structured grids. The time integration is carried out by means of the second-order-accurate backward scheme of Gear. The spatial scheme is a modified low-dissipative AUSM+(P) scheme (Mary & Sagaut 2002). Further details concerning the numerical method and implementation of turbulence models can be found in references Péchier, Guillen & Caysac (2001), Deck *et al.* (2002). The accuracy of the solver for DNS, large eddy simulation (LES) and hybrid Reynolds-averaged Navier–Stokes (RANS)/LES purposes has been assessed in various applications including transitional flows (Mary & Sagaut 2002), wall-bounded turbulent flows (Deck *et al.* 2011; Gand *et al.* 2010; Pamiès *et al.* 2009) as well as separated flows (Dandois, Garnier & Sagaut 2007; Deck & Thorigny 2007; Larchevêque *et al.* 1997; Simon *et al.* 2007; Weiss *et al.* 2009; Weiss & Deck 2011). In these last references, the numerical results are thoroughly compared with the available experimental data of the near-field fluctuations including spectral and second-order analysis.

The zonal detached-eddy simulation (ZDES) was first proposed by Deck (2005*a*,*b*) and the complete formulation has been recently published in (Deck 2012). In this method, which belongs to the family of multi-resolution approaches (see for instance the discussion by Sagaut, Deck & Terracol 2013), a different hybrid length scale is defined according to the type of flow treated: mode 1 concerns flows where the separation is triggered by a relatively abrupt variation in the geometry; mode 2 is when the location of separation is induced by a pressure gradient on a gently curved surface and mode 3 is for flows where the separation is strongly influenced by the dynamics of the incoming boundary layer. The present study only requires the use of the mode 3 branch of the ZDES approach (Deck 2012). The ability of ZDES to operate in wall-resolved large eddy simulation (WRLES) as well as in wall-modelled LES (WMLES) mode has been demonstrated in Deck *et al.* (2011), Laraufie, Deck & Sagaut (2011, 2012), Laraufie & Deck (2013), Deck & Laraufie (2013). Even though the WRLES approach cannot be considered as a direct numerical simulation, the high resolution of the mesh and the nature of the analysis performed in the present study make the contribution of the subgrid-scale modelling strategy negligible to the conclusions drawn in the following analysis of mean wall shear stress. This will be shown later in this paper, especially in figures 13 and 16, revealing that the weight given to the outer layer in the FIK identity justifies the possibility of modelling to some extent the near-wall dynamics.

As soon as the boundary layer is partly resolved in the LES mode, a turbulent content has to be injected at the inlet of the domain in order to prevent turbulence decay, which may lead to relaminarization. An adaptation of the synthetic eddy method of Jarrin *et al.* (2006), proposed by Pamiès *et al.* (2009) and extended to ZDES by Deck *et al.* (2011), is adopted for this purpose.

2.2. *Grids and description of the computation*

The test case is a spatially developing zero-pressure-gradient turbulent boundary layer over a smooth flat plate. The free-stream velocity is $U_\infty = 70\,\mathrm{m\,s^{-1}}$, with the corresponding Mach number $M_\infty = 0.21$; the static pressure is set to $P_\infty = 99\,120\,\mathrm{Pa}$, the temperature equals 287 K leading to a Reynolds number per metre $Re = 4.72 \times 10^6\,\mathrm{m^{-1}}$. A no-slip adiabatic boundary condition is applied at the wall.

Δx	Δy	Δz	$N_y^{\delta_{13\,000}}$	$N_x \times N_y \times N_z$
50^+	1^+	12^+	125	$5950 \times 204 \times 660$
$0.050\delta_0$	$0.00100\delta_0$	$0.0130\delta_0$		
$0.013\delta_{13\,000}$	$0.00026\delta_{13\,000}$	$0.0032\delta_{13\,000}$		

TABLE 2. Parameters of the grid. N_x, N_y and N_z are the grid sizes along the axes and the Δ are the corresponding resolutions expressed in both inlet wall units (superscript +) and inlet boundary layer thickness units (δ_0). $\delta_{13\,000}$ is the boundary layer thickness at $Re_\theta = 13\,000$ and $N_y^{\delta_{13\,000}}$ is the number of points in the wall-normal direction clustered in $\delta_{13\,000}$.

The initial boundary layer thickness is $\delta_0 = 5.82$ mm so that $Re_{\delta_0} = 27\,165$. The outer scales are given by the free-stream velocity and the 99 % boundary layer thickness δ. Based on the two-dimensional mean velocity profile $\langle u \rangle(x, y)$, the shear stress at the wall τ_w is obtained as $\tau_w(x) = (\mu(\mathrm{d}\langle u \rangle/\mathrm{d}y))_{y=0}$ where $\mu = \rho\nu$ is the molecular viscosity given by Sutherland's law, with ρ the density and ν the kinematic viscosity. The relevant velocity and length scales close to the wall are thus $u_\tau = \sqrt{\tau_w/\rho_w}$ and $l_\nu = \nu_w/u_\tau$. It has been checked that because of the low free-stream Mach number, the turbulence dynamics is almost incompressible, and the variations of the mean density are less than 1 % across the boundary layer, which implies that the mean flow may be considered incompressible as well. The variations of the mean viscosity are also less than 1 %. The data presented in the following will accordingly be compared to incompressible simulations and very low-Mach-number experiments without any rescaling. Quantities in wall scaling are written as $u^+ = u/u_\tau$ and $y^+ = y/l_\nu$.

The computational domain sizes in the streamwise, spanwise and wall-normal directions are respectively $L_x = 342\delta_0$, $L_z = 8.6\delta_0$ and $L_y = 41\delta_0$ so that the range of Reynolds number covered by the simulation is $3060 \leqslant Re_\theta \leqslant 13\,650$ ($1070 \leqslant Re_\tau \leqslant 3800$). The large range of Reynolds numbers simulated provides the required space for the streamwise stretched large-scale structures to develop without any spurious perturbation that could be caused by too short a domain. As mentioned in the introduction, the largest coherent structures may be up to 15 boundary layer thicknesses long, which calls for a long domain for the proper resolution of the boundary layer dynamics in the streamwise direction. The major parameters of grid resolution are gathered in table 2 and can be compared with those used in previous numerical studies in table 1. The values in wall units refer to the boundary layer at the inlet of the computational domain. Since the mesh has uniform spacings along the streamwise direction, this means that the mesh spacings in wall units at the outlet of the numerical domain are slightly smaller than the values given in table 2, because of the spatial development of the boundary layer. However, this does not result in significantly smaller values. Besides, the mesh resolution and isotropy in the outer region of the boundary layer are very good (see e.g. the number of grid points $N_y^{\delta_{13\,000}}$ across the boundary layer thickness given in table 2). It will be shown in § 5 below that the study of mean wall shear stress according to the FIK identity (Fukagata *et al.* 2002), which is the main focus of this simulation, requires a very good resolution of the outer layer, where the terms contributing to mean wall shear stress in the framework of the FIK identity tend to concentrate. On the other hand, the resolution of the inner layer seems to be less crucial, and this motivates the use of a ZDES simulation that does not fully resolve the turbulence dynamics, especially near the wall, unlike a DNS. Some experimental facts suggest that the outer layer dynamics,

when scaled in outer units, is not significantly influenced by the near-wall dynamics, as long as the phenomena taking place near the wall are of a negligible size compared to the outer scales. For example, it is reported in Kunkel & Marusic (2006) that the surface roughness, provided the roughness height is very small compared to the boundary layer thickness, has no major impact on the behaviour of the outer layer, as long as the proper scaling is used.

Because of the challenging CPU cost that the simulation of high-Reynolds-number boundary layers represents, a trade-off was sought between conflicting requirements. Firstly, the mesh resolution in the outer layer has to be fine enough for the proper resolution of the coherent structures that have the strongest impact on mean wall shear stress according to the FIK identity. This implies that the mesh was not coarsened in the wall-normal direction as quickly as it might have been in a simulation designed for another purpose. Consequently, even though the wall-normal resolution was limited near the wall in order to keep the CPU cost of the simulation within reasonable reach, the simulation of the outer layer, which is the main focus of this study, appears to provide a satisfactory resolution, and should not be significantly influenced by possible near-wall inaccuracies, given its weak dependence on the inner layer behaviour as revealed by the experimental comparison between smooth and rough surfaces. Note that for $x/\delta_0 > 383$ (where $Re_\theta = 13\,700$), mesh cells are stretched in order to progressively damp the turbulent fluctuations. This procedure is common to ensure protection of the domain of interest from wave reflections, combined with the subsonic characteristic boundary treatment at the outlet of the numerical domain.

The time step needs to be chosen in order to correctly describe the important physical phenomena which are being simulated. For wall-bounded flows, Choi & Moin (1994) proposed the $\Delta t^+ < 1$ criterion where $\Delta t^+ = u_\tau^2 \Delta t_{CFD}/\nu$ and u_τ and ν denote respectively the friction velocity and the kinematic viscosity, Δt_{CFD} being the time step of the simulation. These authors showed that a time step of size $\Delta t^+ \approx 0.4$ resulted in negligible error in their DNS. In the present study, the physical time step is set to 4.8×10^{-7} s leading to $\Delta t^+ = 0.26$ so that the selected time step satisfies this criterion. After the transient phase, the real unsteady calculation begins, allowing the collection of statistics. The averaging procedure is performed on the fly during the calculation over a total duration of $1155\,\delta_0/U_\infty$ inertial times. To allow the calculation of the premultiplied spectra and streamwise-derivative quantities, selected volumes of the unsteady field have been stored leading to a storage of 3 Terabytes of data. The cost of the calculation is close to 2×10^6 CPU hours on 936 Nehalem processors of the CINES superscalar computer Jade-SGI Altix Ice 8200.

3. Validation

3.1. *Flow visualization*

A first visual impression of the spatially developing boundary layer can be gained from figure 2 where an instantaneous schlieren visualization of the whole domain as well as zoom near $Re_\theta = 13\,000$ are displayed. In the zoom, the boundary layer thickness $\delta(x)$ based on the Reynolds-averaged streamwise velocity is also represented. The heads of some large coherent structures are located well above the conventional $y = \delta$ edge of the boundary layer, in the outer intermittent region. The spatial organization of the turbulent coherent structures suggested by the visualization seems to be in good agreement with models such as the paradigm of the packets of hairpins (Adrian *et al.* 2000). The measured mean inclination angle of the coherent patterns is in good agreement with the angle reported in Marusic & Heuer (2007), which

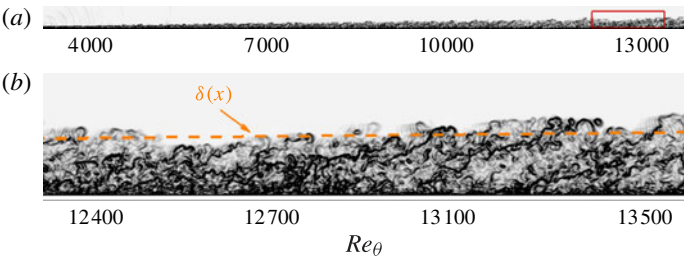

FIGURE 2. (Colour online) Instantaneous schlieren $Sch\,(x, y) = \left((\partial\rho/\partial x)^2 + (\partial\rho/\partial y)^2\right)^{1/2}$; (*b*) shows a zoom of a small rectangular region in (*a*) to highlight the flow around $Re_\theta \approx 13\,000$. Boundary layer thickness δ based on Reynolds-averaged streamwise velocity shown as the dashed line.

is close to 14°. In figure 2 the largest structures are inclined at an angle ranging from 14° to 24°, with an average value close to 19°. Several reasons why this angle is slightly larger than in the experiments can be put forward. Firstly, the angle is not determined in the same way. A typical experimental measurement relies on the search for the maximum correlation coefficient between the streamwise velocity signals recorded at two different heights in the boundary layer at the same x location. The corresponding time lag is then converted into a spatial lag by Taylor's hypothesis of frozen turbulence, using the Reynolds-averaged velocity as the convection velocity. In contrast with this experimental measurement, the angles reported here for the ZDES simulation were directly measured on the numerical schlieren. A second reason for the difference between the measured angles could originate from the possible confusion between the angle of a single, smaller-scale, hairpin and the angle associated with the spatially coherent hairpins that form a large-scale packet, as emphasized in Marusic & Heuer (2007).

Another insight into the global organization of the flow is provided by the Q criterion, one isosurface of which is plotted in figure 3 coloured by the streamwise velocity. The evolution of the typical coherent structures is emphasized by five insets extracted at different Reynolds numbers. As expected, the structures do not look very coherent and well defined, because of the relatively high Reynolds numbers. Hairpins probably only exist as the average addition of many structures of various scales, which makes it very hard to recognize any hairpins. This had already been emphasized in Jiménez *et al.* (2010), where packets of hairpins proved difficult to see.

Also, one striking feature appearing at higher Reynolds numbers is the presence of very large scales, elongated and somewhat meandering areas in which the density of coherent structures seems to be higher than the average in the outer layer and lower than the average in the inner layer. The structures in the outer layer are green and orange (high streamwise velocity) whereas those in the inner layer are blue (low velocity). These areas might be attributed to the so-called very large-scale motions, or superstructures. They consist of a streamwise velocity globally lower than the average at some height above the wall. Because the outer velocity is constant, equal to the free-stream velocity, this results in a higher shear stress in the outer layer, producing higher turbulent intensities. Conversely, this results in a lower shear stress near the wall, since the no-slip condition still holds at the wall. Consequently, there is less turbulent kinetic energy production in the inner layer. On each side of these large-scale

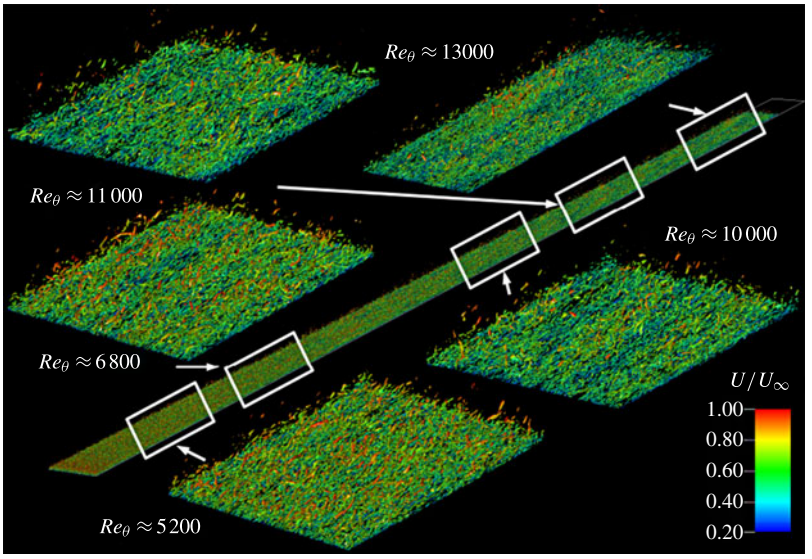

FIGURE 3. (Colour online) Isosurface of the non-dimensionalized Q criterion $Q(\delta_0^2/U_\infty^2) = 0.5$ coloured by the streamwise velocity.

structures there seems to be, on the contrary, high-speed areas. These areas feature higher shear and turbulent kinetic energy near the wall (blue structures) and lower shear and turbulent kinetic energy in the outer layer. Since there are less green and orange structures, these areas are seen as 'blue' areas in figure 3.

Figure 4 shows velocity fluctuation contours in a wall-parallel plane in the buffer layer at $y^+ = 20$. Clearly visible in figure 4(*a*) is a two-scale organization of the streamwise velocity fluctuations with high- and low-momentum streaks of width $O(100\,l_\nu)$ characterizing the inner layer turbulence and very long regions of negative u fluctuation, visible in the plot as elongated dark regions. These very large scales maintain a footprint in the near-wall region as is now commonly acknowledged. Streamwise length scales $O(5\delta$–$6\delta)$ with a characteristic width of approximatively 0.3δ can be distinguished. These characteristics agree well with previous experimental (Hutchins & Marusic 2007) or DNS (Lee & Sung 2011; Pirozzoli & Bernardini 2013) observations.

Instantaneous views of the spanwise velocity fluctuation w' displayed in figure 4(*b*) suggest that these superstructures may affect the spanwise velocity, but not in an obvious manner. They indeed suggest that these superstructures meander significantly along their length. Some structures, shorter than those featured in the u' plot, may be guessed from the spanwise velocity fluctuations. Moreover, the width of these regions seems to be of the same order of magnitude as found in the literature, i.e. 0.3δ, for the larger scale structures of u', suggesting they may be related to each other. However, in an analogous way to particle image velocimetry (PIV) observations reported in a supersonic boundary layer by Ganapathisubramani, Clemens & Dolling (2006) (see figure 2 in that reference), the spanwise velocity fluctuations seem to be much less coherent than their streamwise counterparts, with fewer visible large length scales.

It should be noted that the very large-scale structures would probably be better revealed if a more sophisticated post-processing algorithm were applied, such as the

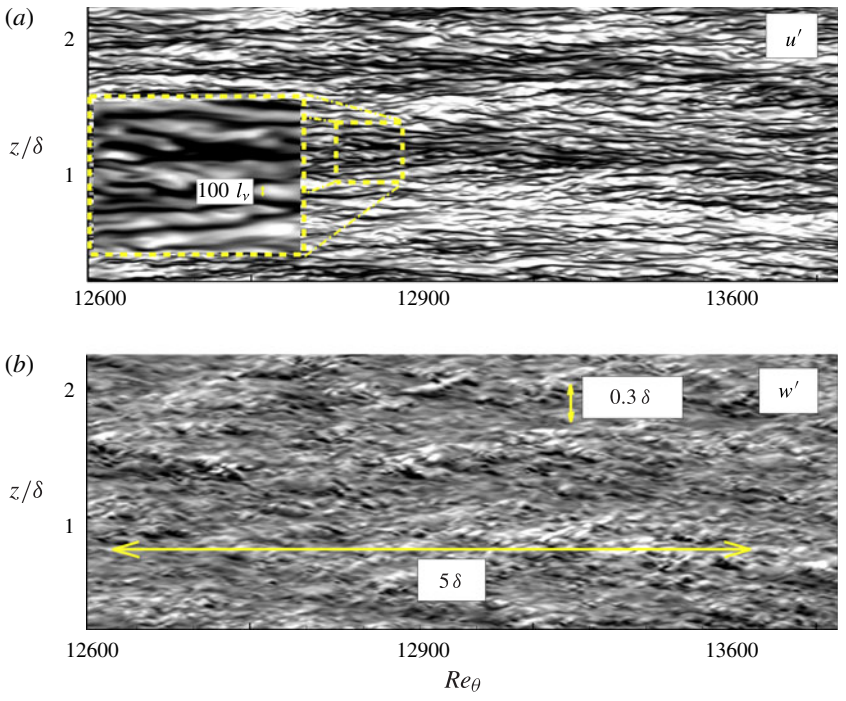

FIGURE 4. (Colour online) Instantaneous flow field in the x–z plane at $y^+ = 20$ around $Re_\theta \approx 13\,000$. ($a$) Instantaneous streamwise velocity fluctuations u'. The inset shows a zoom of a small rectangular region, shown dashed, to highlight the turbulent fine scales (l_ν denotes the viscous length scale). Contour levels are shown for $-0.15 \leqslant u'/U_\infty \leqslant 0.15$ from dark to light shade. (b) Instantaneous spanwise velocity w' fluctuations. Contour levels are shown for $-0.1 \leqslant w'/U_\infty \leqslant 0.1$ from dark to light shade.

skeletonization method presented in Marquillie, Ehrenstein & Laval (2011). However, this is beyond the scope of the present study.

The contribution of these large scales to streamwise velocity fluctuations and mean wall shear stress will be discussed in the following.

3.2. *Global parameters*

The skin friction coefficient C_f from the present calculation is compared in figure 5 with the one given by a RANS calculation using the Spalart–Allmaras model on the same mesh as the present ZDES, and with the friction law by Schlichting based on the 1/7-power law of the velocity profile. Also shown are two correlations from experimental data, one by Michel, Quémard & Durant (1969) based on high-Reynolds-number data, and the modified Coles–Fernholz correlation given in Nagib, Chauhan & Monkewitz (2007) which was fitted to high-Reynolds-number experimental data as well. Moreover, statistics obtained from several DNS and experimental data sets pertaining to a canonical turbulent boundary layer (TBL) under zero pressure gradient are compiled and compared to the present calculation. It is worth noting that the scatter in the experimental data is large partly because most of the skin friction values have been extracted by indirect methods (see some comments on this issue in Nagib *et al.* 2004). Another source of possible scatter in

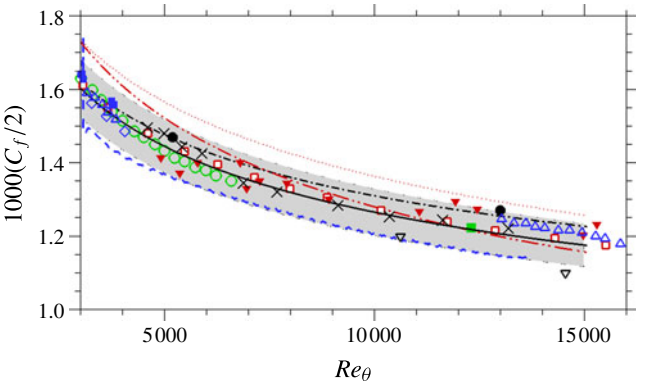

FIGURE 5. (Colour online) Streamwise evolution of the skin friction coefficient (see table 3 for explanation of symbols). The grey area represents the 5 % tolerance limits of the Coles–Fernholz correlation calibrated by Nagib *et al.* (2007).

experimental data comes from the difficulty in designing a test case with perfectly zero pressure gradient, as the spatially growing boundary layer gradually increases wind tunnel blockage, as for instance reported in DeGraaff & Eaton (2000). It is not only the actual values of C_f that differ (up to 5–10 % for the same Re_θ), but also inconsistent trends with respect to Re_θ can be pointed out among the reference data available. Interestingly, Schlatter & Örlü (2010*a*) reviewed DNS datasets and reported that the scatter in the DNS data (up to 5–10 % for the same Re_θ) is as large as in similar experimental compilations. The highest-Reynolds number DNS data and the experiment of Österlund *et al.* (2000) fall closer to the Coles–Fernholz correlation. The friction coefficient for the present simulation was computed from second-order evaluation of the wall-normal derivative of the streamwise Reynolds-averaged velocity at the wall. Care was also taken that the computational domain be large enough in the wall-normal direction, so that possibly imperfect boundary conditions on the upper edge of the domain would not result in a non-zero streamwise pressure gradient caused by a phenomenon analogous to wind tunnel blockage.

C_f of the present calculation is in very good agreement with the one given by the Coles–Fernholz correlation and the discrepancy is of the order of 5 % which is actually very similar to the one observed between two experimental data sets at the same Reynolds number or between the RANS calculation and the Coles–Fernholz correlation.

Also, the wide range of Reynolds numbers of the simulation enables the assessment of the relation between Reynolds numbers Re_θ and Re_τ which is shown in figure 6 together with several experimental datasets and the RANS simulation. The ZDES simulation is in good agreement with the experimental data. The experimental data from DeGraaff & Eaton (2000) suggest a slightly different relation, which is actually closer to the RANS simulation prediction, but as mentioned earlier, this could be attributed to the pressure gradient issue raised by the wind tunnel blockage. It should also be noted that the experimental data are increasingly scattered for increasing Reynolds numbers, probably as a consequence of the growing difficulty in performing a reliable measurement as the Reynolds number becomes larger. The linear behaviour between the two Reynolds numbers plotted in logarithmic scales suggests a power-law relation. Such a relation is of high practical interest since it makes easier to convert

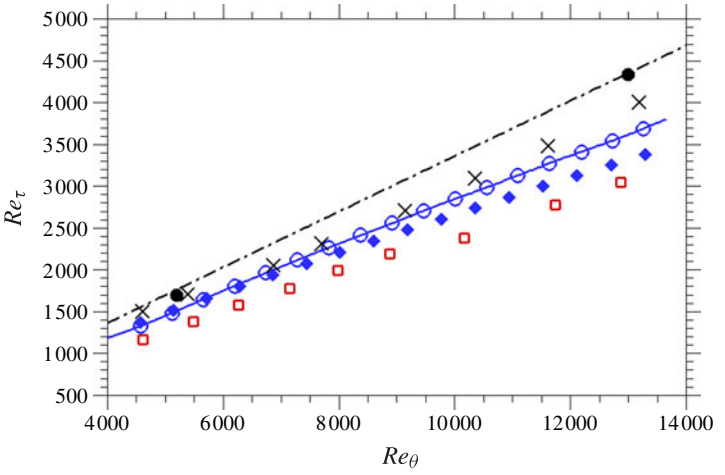

FIGURE 6. (Colour online) Relation between Reynolds numbers Re_θ and Re_τ. ——, present ZDES; ○, best fit to present data, $Re_\tau = 0.435 Re_\theta^{0.954}$; ⧫, best fit from DNS data in the range $300 \leqslant Re_\theta \leqslant 3500$ provided by Schlatter & Örlü (2010*a*),$Re_\tau = 1.13 \times Re_\theta^{0.843}$; – · –, RANS; •, exp. DeGraaff & Eaton (2000);□, exp. Österlund *et al.* (2000);×, exp. Smith (1994).

Reference	Exp./DNS/Correlation	Symbol
DeGraaff & Eaton (2000)	Exp.	•
Österlund *et al.* (2000)	Exp.	□
Fernholz & Finley (1996)	Exp.	▼
Head & Bandyopadhyay (1981)	Exp.	▽
Nagib *et al.* (2007)	Exp.	■
Smith (1994)	Exp.	×
Erm & Joubert (1991)	Exp.	■
Schlatter & Örlü (2010*a*)	DNS	◇
Pirozzoli & Bernardini (2013)	DNS	△
Sillero *et al.* (2011)	DNS	◯
Coles–Fernholz, best fit from Nagib *et al.* (2007)	$C_f = 2\left(\frac{1}{0.384}\ln(Re_\theta) + 4.127\right)^{-2}$	——
Schlichting (1968)	$C_f = 0.0256 Re_\theta^{-1/4}$	– · · –
Michel *et al.* (1969)	$C_f = 0.0172 Re_\theta^{-1/5}$	· · · ·
Spalart & Allmaras (1992)	RANS	– · –
Present	ZDES	– – –

TABLE 3. List of symbols utilized in figures 5 and 7.

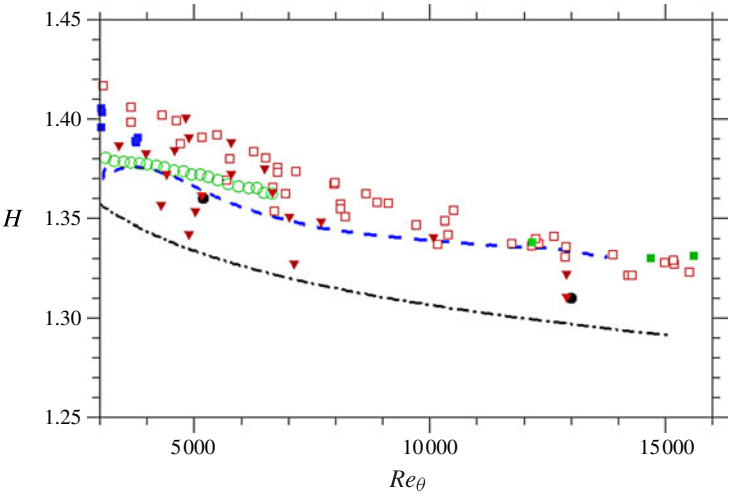

FIGURE 7. (Colour online) Streamwise evolution of the shape factor (see table 3 for explanation of symbols).

between the two Reynolds numbers. The best fit to our data provides the following relation:

$$Re_\tau = 0.435\, Re_\theta^{0.954}. \tag{3.1}$$

This is in good agreement with the best fit from data in the lower-Reynolds-number range $300 \leqslant Re_\theta \leqslant 3500$ provided by Schlatter & Örlü (2010*a*), namely $Re_\tau = 1.13 \times Re_\theta^{0.843}$, which is also plotted in figure 6.

The shape factor $H = \delta_1/\theta$ gives another assessment of the mean velocity profile independent of the skin friction (i.e. wall-normal derivative). The computation of H relies on the evaluation of two integral quantities which may be less sensitive to numerical or experimental inaccuracies than the evaluation of skin friction. The values obtained by the present calculation are given in figure 7. Let us be reminded that the 1/7-power law of the velocity profile proposed by Schlichting (1968) yields $H = 1.285$ which is significantly lower than the values observed at high Reynolds number. This result corroborates the deviations in C_f observed by Schlichting's law in figure 5. Most interestingly, the trend observed in the experimental and DNS data is very well reproduced by the ZDES simulation: the shape factor decreases gradually for increasing Reynolds numbers, as emphasized and predicted by theoretical considerations in Nagib *et al.* (2007). The level of H in the ZDES simulation is in good agreement with the somewhat scattered reference data available. The maximum Reynolds number achieved is not high enough to confirm that H should decrease below 1.3 and even tend towards 1 for infinite Reynolds numbers as the theory given in Nagib *et al.* (2007) predicts with some experimental support. Higher-Reynolds-number simulations are needed for such purposes.

Another parameter of interest for the turbulent boundary layer is Coles' wake factor Π initially defined by Coles (1956), which is related to the wake profile of the boundary layer (outer region beyond the logarithmic layer) and has by definition a constant value in an equilibrium turbulent boundary layer. This constant value is close to 0.55 for a zero-pressure-gradient boundary layer for any high enough Reynolds number, according to Nagib *et al.* (2007). Checking that the wake factor keeps a

constant value over the simulated range of Reynolds numbers reveals whether the simulated boundary layer has reached equilibrium or not, thus assessing the quality of the numerical method. However, computing the wake factor can be done in several ways, depending on the assumptions made in the wake and wall laws. Consequently, different expressions can be found, e.g. in Coles (1956), in Perry, Marusic & Jones (2002) and in Nagib *et al.* (2007), leading to somewhat different levels but a globally unchanged trend of the wake factor evolution with respect to the Reynolds number. Here the wake factor Π_{99} computed according to the method presented in Nagib *et al.* (2007) is presented and compared to the set of experimental data gathered in the same reference. The starting point is the velocity profile law assumed to be valid in the whole boundary layer except in the viscous sublayer and buffer layer by Coles (1956):

$$\frac{\langle u\rangle}{u_\tau} = \frac{1}{\kappa}\ln\left(\frac{yu_\tau}{\nu}\right) + A + \frac{\Pi}{\kappa}w\left(\frac{y}{\delta}\right), \tag{3.2}$$

where $\langle u\rangle(y=\delta) = U_\infty$, $\langle u\rangle(y=\delta_{99}) = 0.99U_\infty$ and $w(1)=2$ by definition. From this expression, Π is derived in Coles (1956) by assuming that the given law is valid down to the wall, thus neglecting the viscous effects. In Nagib *et al.* (2007), the authors instead use this law only where it is valid, eventually only at $y=\delta_{99}$, which yields:

$$\Pi_{99} = \frac{\kappa}{w(\delta_{99}/\delta)}\left(0.99\frac{U_\infty}{u_\tau} - \frac{1}{\kappa}\ln\left(\frac{\delta_{99}u_\tau}{\nu}\right) - A\right) \approx \frac{\kappa}{2}\left(0.99\frac{U_\infty}{u_\tau} - \frac{1}{\kappa}\ln\left(\frac{\delta_{99}u_\tau}{\nu}\right) - A\right), \tag{3.3}$$

where $w\,(\delta_{99}/\delta)$ has been replaced with $w(1)=2$ because the actual wake function w has a first derivative with respect to y close to 0 at $y=\delta$, which implies that the approximation $w\,(\delta_{99}/\delta)\approx 2$ is fairly good, while the 0.99 factor present in the equation should on the other hand be kept. As explained in Nagib *et al.* (2007), this relation is used to compute Π_{99} from the measured δ_{99} and Re_{δ_1} (δ_{99} is explicitly computed as the location where the Reynolds-averaged streamwise velocity is equal to 0.99 times the outer velocity, whereas δ_1 is evaluated by numerical integration of the velocity profile). The values for the constants are, from Nagib *et al.* (2007), $\kappa = 0.384$ and $A = 4.173$. In order to evaluate the required value of U_∞/u_τ, the Coles–Fernholz correlation from Nagib *et al.* (2007) is used so that comparison with the experimental data gathered in the reference is possible:

$$\frac{U_\infty}{u_\tau} \approx \frac{1}{\kappa}\ln(Re_{\delta_1}) + C^*, \tag{3.4}$$

where $C^* = 3.354$. It should be noted that following rigorously this procedure was required in order to make the comparison with available data possible, because of the high sensitivity of the wake factor to the way it is computed. Besides, resorting to a correlation giving the friction coefficient as a function of Re_{δ_1} tends to reduce the scatter of the available data, especially because experimental measurement of the displacement thickness seems to be more accurate than experimental measurement of skin friction. It can be seen in figure 8 that the wake factor Π_{99} computed for the ZDES simulation is in very good agreement with the experimental data from Nagib *et al.* (2007), and that it keeps a nearly constant value suggesting that the simulated boundary layer actually is in an equilibrium state. The value is close to 0.55 which was also the value found in Nagib *et al.* (2007).

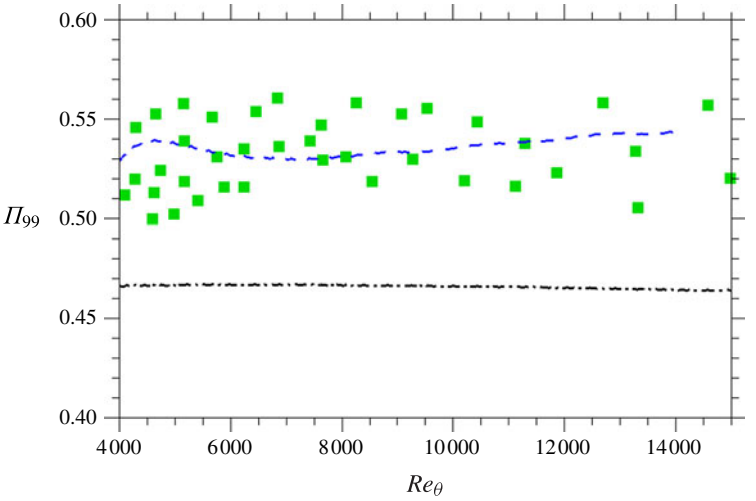

FIGURE 8. (Colour online) Streamwise evolution of Coles wake factor Π_{99} computed according to (3.3) and (3.4) (see table 3 for explanation of symbols).

3.3. *Velocity profiles*

The mean velocity profiles are plotted in outer and inner scales at two different Reynolds numbers in figure 9. The external unit is preferred since this scaling is the one used in the FIK identity (see § 5). The second-order velocity fluctuation statistics at $Re_\theta = 5200$ and 13 000 are shown in the same figure in both inner and outer coordinates. The moments correspond to the resolved fluctuations only. Contrary to the Reynolds shear stress, the modelled part of the normal Reynolds stresses cannot be reconstructed, because the simulation resorts to Boussinesq's eddy viscosity hypothesis for subgrid-scale modelling together with a model for the eddy viscosity itself (there is no prediction of the modelled turbulent kinetic energy in the framework of the one-equation Spalart–Allmaras model). We also show experimental data by DeGraaff & Eaton (2000) and the prediction by the model of Marusic *et al.* (1997), Marusic & Kunkel (2003) of the Reynolds stresses for which experimental data are missing. Deviations are observed in the inner layer, where the present simulation does not perfectly match the experimental data. Significant deviations observed in the inner layer have also been reported by Pirozzoli & Bernardini (2013) in their DNS data at similar Reynolds numbers. On the contrary, the velocity variances are well predicted in the outer layer. As emphasized before, the role played by turbulence modelling in the inner layer has negligible impact on the following analysis of mean wall shear stress. Indeed, the FIK identity weights the outer layer using the wall distance, making the role played by the inner layer in the integral negligible (see figure 16). The mean velocity profiles also feature an accurate wake profile and a substantial logarithmic zone with the proper slope, while the inner layer deviates from the experimental data. The plots in wall units present a slight shift of the curves caused by the underestimation of the friction coefficient in the present simulation, since $U_\infty/u_\tau = \sqrt{2/C_f}$. The proper resolution of the outer layer enables an accurate evaluation of its contribution to the mean skin friction using the FIK identity.

Also, it can be shown that in agreement with the predictions of the attached eddy hypothesis, the spanwise fluctuations feature a logarithmic layer, the width of which

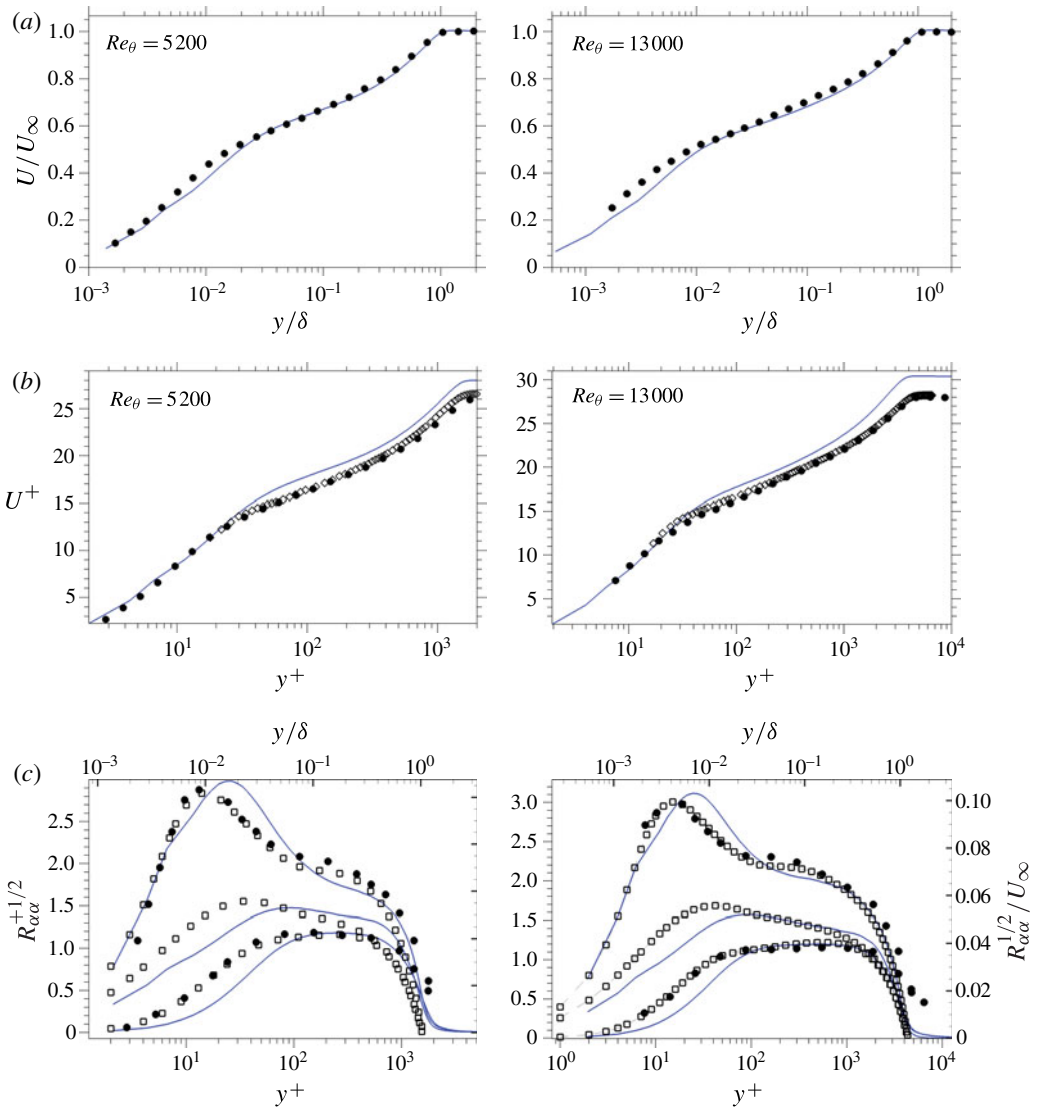

FIGURE 9. (Colour online) (*a*) Mean velocity profiles in outer scale: •, exp. DeGraaff & Eaton (2000); ——, present ZDES. (*b*) Mean velocity profiles in wall units: •, exp. DeGraaff & Eaton (2000); ◇, exp. Smith (1994) at $Re_\theta = 5\,021$ and $Re_\theta = 13\,052$; ——, present ZDES. (*c*) Distribution of normal Reynolds stress components: •, exp. DeGraaff & Eaton (2000); □, model by Marusic, Uddin & Perry (1997), Marusic & Kunkel (2003); ——, present ZDES. Data for two different Reynolds numbers, $Re_\theta = 5200$ (left) and $Re_\theta = 13\,000$ (right).

increases with the Reynolds number. As in Pirozzoli & Bernardini (2013), such a feature is missing for the streamwise velocity fluctuations, although predicted by the attached eddy theory. This is consistent with recent experimental measurements by Hultmark *et al.* (2013) and Marusic *et al.* (2012) that emphasized that the logarithmic layer for streamwise velocity fluctuations appears clearly only at high Reynolds numbers $Re_\tau > 10\,000$, above the Reynolds numbers considered here. Besides, the

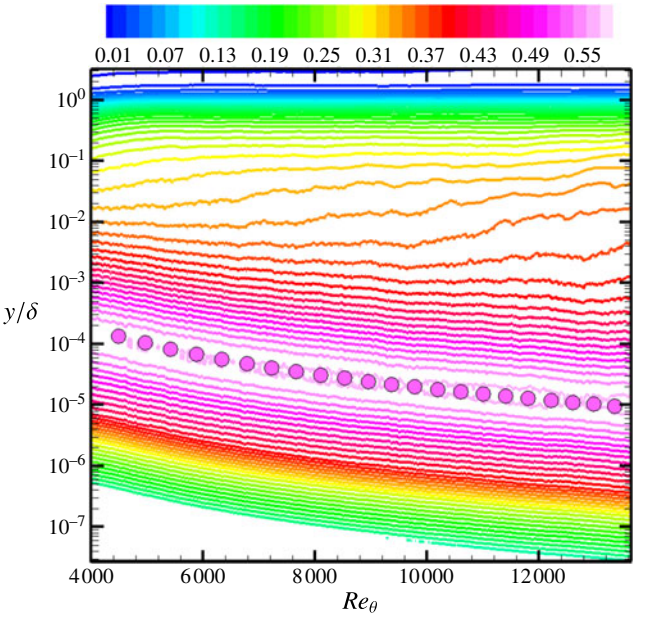

FIGURE 10. (Colour online) Streamwise evolution of the longitudinal velocity fluctuations $(\langle u'^2\rangle/(U_\infty u_\tau))^{1/2}$ for the ZDES simulation (contour lines) together with the correlation of the peak streamwise turbulent intensity given in Hutchins *et al.* (2009) (filled circles).

relative intensity of the streamwise velocity fluctuations in the logarithmic layer clearly increases with the Reynolds number. Above the inner peak, a plateau is growing and could even possibly lead to an outer peak at higher Reynolds numbers which are beyond reach of the present simulation.

DeGraaff & Eaton (2000) emphasized that the longitudinal Reynolds stresses lack universality in inner scaling. The fluctuation amplitudes slowly increase with Re_θ if they are scaled using only the friction velocity u_τ. Figure 10 displays the streamwise evolution of the longitudinal velocity fluctuations in mixed-outer coordinates $\sqrt{\langle u'^2\rangle/(U_\infty u_\tau)}$. This scaling was introduced by DeGraaff & Eaton (2000) and it can be seen that it provides an almost constant value of the maximum streamwise turbulence intensity. The physical justification for this mixed velocity scaling comes from the energy balance of the boundary layer, as detailed in DeGraaff & Eaton (2000). Since the total power dissipated by the boundary layer scales on $U_\infty \tau_w$, for a constant-density flow, the total rate of energy dissipation by turbulence depends on both U_∞ and u_τ. More specifically, the mean specific turbulent kinetic energy (i.e. per unit mass) in the inner region of the boundary layer can be shown to be proportional to $U_\infty u_\tau$ by means of dimensional analysis. Another way of addressing the issue of the level of the inner streamwise velocity fluctuations peak is given by the attached eddy hypothesis of Townsend (1976). As described in Perry & Marusic (1995), the profile of streamwise turbulence intensity predicted by the hypothesis behaves like:

$$\frac{\langle u'^2\rangle}{u_\tau^2} = B_T - A_T \ln\left(\frac{y}{\delta}\right). \tag{3.5}$$

This version of the theory bound to the attached eddy hypothesis does not take into account the viscous effects that are dominating in the closest vicinity of the wall. This means that the above formula should not be used down to the wall, where viscous effects may not be neglected any more. However, the distance to the wall measured in wall units $y^+ = yu_\tau/\nu$ is also the Reynolds number associated with the attached eddies of size y at the height y with typical induced velocity u_τ. Hence, the height from which the viscous effects cannot be neglected any more in the attached eddy hypothesis probably is a constant y^+ value. Consequently, the evolution of the maximum value of $\langle u'^2\rangle$ with Reynolds number could be evaluated from equation (3.5) at the height $y^+ = 15$ where experiments indicate that the maximum is located. This provides the following prediction of the peak $\langle u'^2\rangle$:

$$\frac{\langle u'^2\rangle_{peak}}{u_\tau^2} = B_T + A_T \ln\left(\frac{Re_\tau}{15}\right). \tag{3.6}$$

As mentioned in Hwang (2013), this relation is equivalent to the mixed scaling suggested by DeGraaff & Eaton (2000) $\langle u'^2\rangle_{\text{peak}} \sim U_\infty u_\tau$ as soon as $U_\infty \sim u_\tau \ln(Re_\tau)$, which can also be formulated as $C_f \sim (\ln(Re_\tau))^{-2}$. In figure 10, we also consider the peak streamwise velocity variance as a function of Re_θ and compare with the correlation derived in Hutchins *et al.* (2009) from the prediction from the Townsend (1976) attached eddy hypothesis fitted to experimental data by Hutchins *et al.* (2009), namely:

$$\frac{\langle u'^2\rangle_{peak}}{u_\tau^2} = 4.837 + 0.469 \ln(Re_\tau). \tag{3.7}$$

Figure 10 suggests that we recover logarithmic growth of the velocity variance and that this growth is fully compatible with the mixed scaling by DeGraaff & Eaton (2000). Also, this figure reveals the growth of a plateau of $(\langle u'^2\rangle/(U_\infty u_\tau))^{1/2}$ in the outer region of the boundary layer, which possibly would result in an outer peak at higher Reynolds numbers. It can be seen that with the distance to the wall scaled in boundary layer thickness (outer scaling), the inner peak moves closer to the wall when the Reynolds number increases, which is not surprising since it is located at an approximately constant position in inner scaling. On the other hand, it can be seen that the contour lines corresponding to given levels of streamwise fluctuations in mixed scaling clearly move towards the edge of the boundary layer in outer distance scale for Reynolds numbers higher than $Re_\theta \approx 7000$. This shows again how the plateau gradually grows for increasing Reynolds numbers.

3.4. *Spectral analysis of the streamwise fluctuations*

To gain a better insight into the contribution of each streamwise length scale to the streamwise velocity fluctuations, spectra across the boundary layer are shown in figure 11. The figure shows contours of the one-sided premultiplied one-dimensional streamwise power spectral density of the resolved streamwise velocity non-dimensionalized by the friction velocity $k_x\Phi_{uu}/u_\tau^2$ versus λ_x/δ and y/δ for $Re_\theta = 5200$ and 13 000. $k_x\Phi_{uu}$ is normalized so that:

$$\langle u'^2\rangle = \int_0^\infty \Phi_{uu}(k_x)\,\mathrm{d}k_x = \int_{-\infty}^{\infty} k_x\Phi_{uu}(k_x)\,\mathrm{d}\ln(k_x). \tag{3.8}$$

This equation shows that the contribution of each length scale to the streamwise turbulent intensity is directly proportional to the area below the $k_x\Phi_{uu}$ versus $\ln(k_x)$

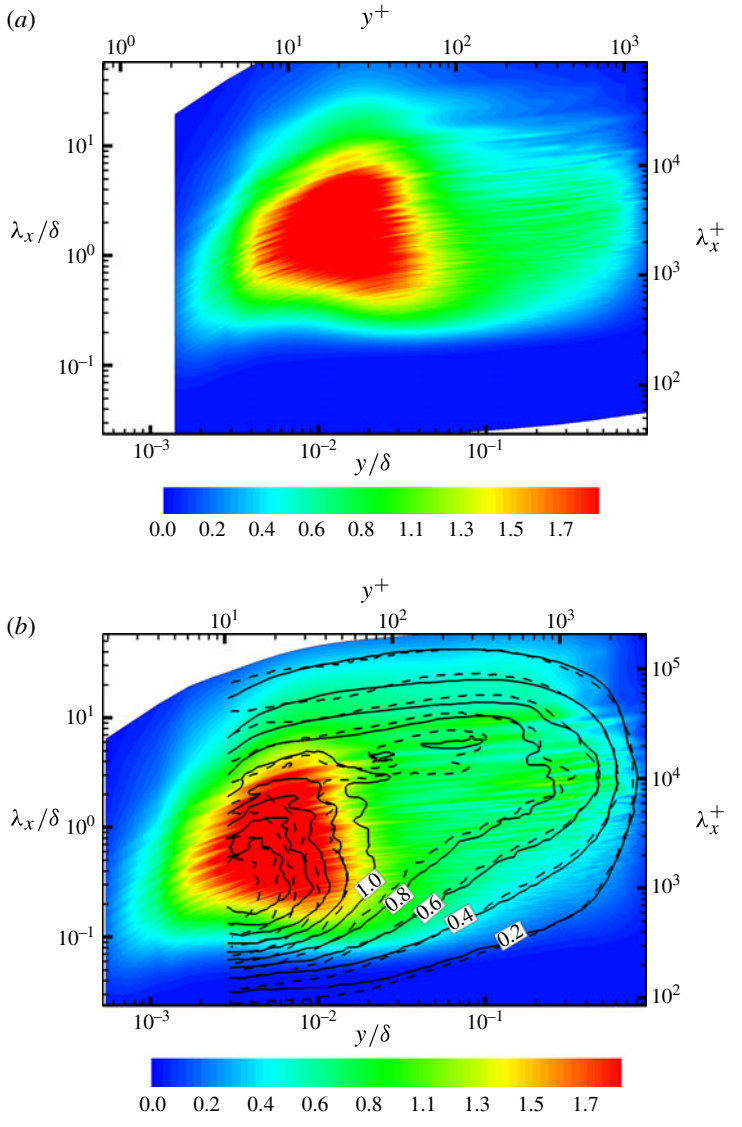

FIGURE 11. (Colour online) Premultiplied power spectral density of the streamwise fluctuations of velocity $k_x\Phi_{uu}/u_\tau^2$ (3.8) at $Re_\theta = 5200$ ($Re_\tau = 1510$) (*a*) and $Re_\theta = 13\,000$ ($Re_\tau = 3600$) (*b*). Coloured map from the present simulation. Isolines from experimental data: ——, $Re_\tau = 2800$ from Mathis *et al.* (2009),– – –, $Re_\tau = 3900$ from Marusic *et al.* (2010*a*). Note that the axis in inner units refers to the present simulation only, whereas the experimental data should be read using the outer units together with the present simulation.

curve at a given height y. This implies that figure 11 enables a direct study of the levels and distribution of streamwise turbulent intensity according to the length scale and the location in the boundary layer. It should be noted that because the boundary layer is spatially developing along x, x is not an homogeneous direction. Consequently, the power spectral density shown cannot strictly speaking result from a

Fourier transform along x. Instead, the Fourier transform of a time signal recorded at a given x location is considered. Then the time spectra are converted into spatial spectra according to Taylor's frozen flow hypothesis. It is assumed that the coherent turbulent structures do not evolve much while they are passing the considered x location. If their convection velocity is known, the corresponding spatial shape along x can be deduced from the time signal. This results in a duality between the streamwise wavenumber $k_x = 2\pi/\lambda_x$ and the frequency f according to $\lambda_x = 2\pi/k_x = U_c/f$, where $U_c(y/\delta)$ is the local advection velocity.

In figure 11, the spectrum at $Re_\theta = 13\,000$ is compared with experimental spectra from Mathis *et al.* (2009) and Marusic *et al.* (2010*a*), which were made using the Reynolds-averaged streamwise velocity as U_c. Consequently, the advection velocity is chosen here equal to the Reynolds-averaged streamwise velocity for the purpose of comparison. Other choices can be made, such as computing the advection velocity from the slope of the maximum two-point two-time correlation of streamwise velocity fluctuations. However, different definitions of the advection velocity do not result in significant changes of the spectra, as depicted for instance in Mathis *et al.* (2009). A deeper study of this issue, especially focusing on the impact that Taylor's hypothesis may have on the spectral resolution of the very large-scale structures can be found in Dennis & Nickels (2008). From this reference it can be concluded that wavelengths up to 6 boundary layer thicknesses are properly resolved by the present spectral analysis. Discussions on the dependence of the convection velocity on the size of the coherent structures can be found in Krogstad, Kaspersen & Rimestad (1998) and in del Álamo & Jiménez (2009). One possible limitation of using the Reynolds-averaged streamwise velocity is that the large structures located near the wall tend to be convected at a velocity that does not seem to scale like the friction velocity (as the local mean velocity does). It seems to scale like the outer velocity instead, or as reported in a study by Hutchins *et al.* (2011), like a mixed scaling close to the mean velocity at the geometric centre of the logarithmic layer where $y^+ \approx 3.9\sqrt{Re_\tau}$. This can lead to some underestimation of the size of the largest structures near the wall, more so as the Reynolds number is higher.

It can be seen in figure 11 that a fair agreement between the experimental data and the present results is obtained, especially in the outer layer. The comparison of the spectra at $Re_\theta = 5200$ and $Re_\theta = 13\,000$ shows one very clear inner energy site, but also an outer energy site emerging with increasing Reynolds numbers. The inner site is due to the near-wall cycle of streaks in the buffer layer. As a consequence, its location and the size of the coherent structures it results from tend to scale in inner scales. This explains why its location given in outer scale (y/δ) is moving closer to the wall with increasing Reynolds numbers, and why the peak size, scaled in outer scale λ_x/δ of the structures it is made of, is also decreasing with increasing Reynolds numbers. Both trends are obvious in the experimental data shown in Mathis *et al.* (2009). As the Reynolds number increases, a second energy site emerges in the outer layer. Even though a local maximum of the power spectral density cannot be seen as clearly on the simulation results as with the experimental data, energy is very clearly appearing in the largest scales, outer layer zone of the spectrum, in excellent agreement with the shape of the experimental spectra. This is assumed to be caused by the spectral content of the very large-scale motions that are described in the section on flow visualization.

Equation (3.8) allows the velocity signatures across a boundary layer to be decomposed into small-scale ($\lambda_x < \lambda_c$) and large-scale ($\lambda_x \geqslant \lambda_c$) contributions (Smits *et al.* 2011) by integrating the power spectral density over the small- or large-scale

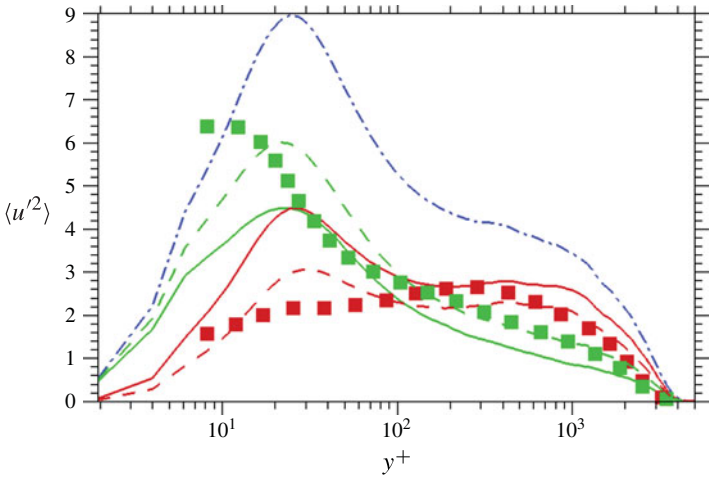

FIGURE 12. (Colour online) Contribution of the large and small scales to the streamwise velocity fluctuations at $Re_\theta = 13\,000$ ($Re_\tau = 3600$): $-\cdot-$, total signal; green solid line, $\lambda_x < \delta$; red solid line, $\lambda_x \geqslant \delta$; green dashed line, $\lambda_x < 2\delta$; red dashed line, $\lambda_x \geqslant 2\delta$. Experimental data from Marusic *et al.* (2010*a*) at $Re_\tau = 3900$: green square, $\lambda_x < \delta$; red square, $\lambda_x \geqslant \delta$.

range of wavelengths defined by the cut-off wavelength λ_c. Typically $\lambda_c = \delta$, which makes the difference between the small viscous-scaled contribution and the larger outer-scaled contribution. In particular, figure 12 indicates that the $\langle u'^2 \rangle$ profile can be considered as the sum of a small viscous-scaled contribution primarily located in the near-wall region and a larger outer-scaled contribution. The resulting profiles are compared with the experimental data from Marusic *et al.* (2010*a*) at a slightly higher skin friction Reynolds number. A second value of the cut-off wavelength is presented, $\lambda_c = 2\delta$. The latter cut-off makes clearer the contribution of the outer layer to the larger-scale fluctuations and of the inner layer to the smaller-scale fluctuations. The profiles for the same cut-off $\lambda_c = \delta$ of the present simulation and of the experimental data do not agree very well, whereas the profiles for the present simulation with $\lambda_c = 2\delta$ are much closer to the experimental ones (for which $\lambda_c = \delta$). This can be partly explained by the different Reynolds numbers. Indeed, as shown in figure 11, the inner energy site at such Reynolds numbers still has a significant footprint on the large-scale domain. Increasing the Reynolds number does increase the energy associated with the outer layer large scales, but also results in a motion of the inner site towards the wall when y is scaled with δ, thus reducing the contribution of this site to the large-scale fluctuations. As a consequence, at the slightly lower Reynolds number of the simulation, a slightly higher cut-off wavelength is required in order to get similar profiles.

Other sources of discrepancy in the cut-off value can also be thought of, such as different methods to estimate the power spectral density which may result in different spectral distortion at low frequencies. It should also be noted that the emergence of the large-scale outer peak and the absence of significant change of the small-scale profile that is shown in Marusic *et al.* (2010*a*) cannot be seen when figure 12 is compared to its equivalent at $Re_\theta = 5200$. Indeed, Marusic *et al.* (2010*a*) deal with Reynolds numbers higher than $Re_\theta = 13\,000$, whereas the present simulation deals with Reynolds numbers smaller than $Re_\theta = 13\,000$, for which the trend is different. The reason for the different trend is that the inner site corresponding to small scales at high

Reynolds numbers actually is located near the large scales site at $Re_\theta = 5200$, as can be seen in figure 11. Increasing the Reynolds number from $Re_\theta = 5200$ to $Re_\theta = 13\,000$ mainly results in moving the inner site with respect to the cut-off wavelength, which is located somewhere inside this site. Consequently, large scales in the inner layer could be believed to be stronger at $Re_\theta = 5200$ than at $Re_\theta = 13\,000$ because the inner fluctuations are mistakenly taken for large scales due to the lack of scale separation at moderate Reynolds numbers. This shows how useful the full spectra are compared to semi-integrated global values.

4. A glimpse into the FIK identity

The FIK identity was first presented in Fukagata *et al.* (2002) as a tool to decompose the turbulent mean friction coefficient of wall-bounded turbulent flows into several contributing terms emphasizing the physical sources of mean friction and their distance from the wall. Indeed, this identity provides a quantity that amounts to the turbulent friction once integrated with respect to the wall distance. To the authors' knowledge, there is no other such quantity available in the literature. For instance, even though the wall-normal derivative of the Reynolds shear stress describes how the mean flow is retarded or accelerated by the turbulent fluctuations, as pointed out by Balakumar & Adrian (2007), it does not seem to be directly related to mean wall shear stress. In particular, the integral of this quantity over the boundary layer thickness vanishes (assuming a zero Reynolds shear stress at $y = \delta$, which is close to the actual value), since:

$$\int_0^\delta \frac{\partial}{\partial y}\left(-\langle u'v'\rangle\right)\,\mathrm{d}y = -\langle u'v'\rangle(\delta) - \left(-\langle u'v'\rangle(0)\right) = 0. \tag{4.1}$$

It can be seen that mean wall shear stress does not result from the integral of the contribution of $(\partial/\partial y)\,(-\langle u'v'\rangle)$ over the boundary layer. Moreover, the term $(\partial/\partial y)\,(-\langle u'v'\rangle)$ has to be positive and negative in different areas of the boundary layer so that its integral vanishes. What could be interpreted as a contribution of the Reynolds shear stress to mean wall shear stress at a given wall distance would be a negative value of $(\partial/\partial y)\,(-\langle u'v'\rangle)$, meaning that the turbulent stress tends to retard the mean flow. This is the case in the outer layer, but on the contrary near the wall this term is positive, so that the overall integral vanishes. It clearly appears that the turbulent fluctuations in the inner layer tend to accelerate the mean flow, but it would seem somewhat misleading if one concluded that the turbulent fluctuations in the inner layer produce negative drag. As explained in Balakumar & Adrian (2007), the co-spectrum of $(\partial/\partial y)\,(-\langle u'v'\rangle)$ has a sign that also depends on the wavelength, but this relates to mean flow retardation or acceleration. The relation to mean wall shear stress generation is not obvious. On the other hand, the FIK identity provides an explicit description of the contribution to mean wall shear stress depending on wall distance.

The FIK identity was generalized to compressible flows in Gomez, Flutet & Sagaut (1981), and to some non-planar walls in Peet & Sagaut (2009). Even though it has been widely used to study turbulent channel flows, for which it shows a direct relationship between the weighted distribution of the Reynolds shear stress across the boundary layer and the mean turbulent friction, less has been written on the use of the FIK identity to analyse the zero-pressure-gradient flat-plate boundary layer. One such analysis can nevertheless be found in Lee *et al.* (2013), but only at moderate Reynolds numbers up to $Re_\theta = 2060$.

In the channel flow case, the term of the FIK identity corresponding to spatial inhomogeneity is zero, and the study of turbulent mean friction generation focuses on the Reynolds shear stress. The study of the spatially developing flat-plate boundary layer usually focuses in an analogous way on the Reynolds shear stress. Yet in the latter case the inhomogeneity term is non-zero, making the relation between the Reynolds shear stress and the mean friction less obvious. This section discusses to what extent the generation of mean skin friction can still be related to the Reynolds shear stress in this case, by considering the behaviour of the terms of the FIK identity at high Reynolds numbers. Some remarkable high-Reynolds-number trends seem to give strong support to the usual focus on the Reynolds shear stress. A physical explanation for these observed trends is then suggested. This leads to the conclusion that the study of the weighted Reynolds shear stress appears to be sufficient for the understanding of turbulent friction generation at high Reynolds numbers. To better understand the contribution of the turbulent coherent structures to mean friction, especially the very large-scale ones, a scale decomposition of the weighted Reynolds shear stress is performed in § 5.

4.1. *The FIK identity in the flat-plate boundary layer case*

A short summary of the FIK identity applied to the case of the incompressible flat-plate boundary layer with no pressure gradient and a no-slip boundary condition at the wall is first given here. More details can be found in Fukagata *et al.* (2002). The generalization to compressible flows presented in Gomez *et al.* (1981) is not used here, because the fluctuating and mean fields both behave in an almost incompressible manner, as emphasized in the simulation overview § 2. Mean wall shear stress τ_w, the skin friction coefficient C_f and the friction velocity u_τ are defined as:

$$\tau_w = \mu \frac{\partial \langle u \rangle}{\partial y}(y=0) \quad \text{and} \quad C_f = \frac{\tau_w}{\frac{1}{2}\rho U_\infty^2} = 2\left(\frac{u_\tau}{U_\infty}\right)^2. \tag{4.2}$$

The boundary layer thickness δ and the related Reynolds number are:

$$Re_\delta = \frac{\delta U_\infty}{\nu} \quad \text{where} \quad \langle u \rangle\,(y=\delta) = 0.99 U_\infty. \tag{4.3}$$

The displacement thickness δ_1 is defined as:

$$\delta_1 = \int_0^\delta \left(1 - \frac{\langle u \rangle}{U_\infty}\right) \mathrm{d}y. \tag{4.4}$$

As shown in Fukagata *et al.* (2002), from the streamwise momentum equation of the Reynolds-averaged Navier–Stokes equations, the FIK identity can be written in the present case as follows:

$$C_f = C_{f,1} + C_{f,2} + C_{f,3}, \tag{4.5}$$

$$C_{f,1} = \frac{4(1-\delta_1/\delta)}{Re_\delta}, \tag{4.6}$$

$$C_{f,2} = -4\int_0^1 \frac{\langle u'v' \rangle}{U_\infty^2}\left(1 - \frac{y}{\delta}\right) \mathrm{d}\left(\frac{y}{\delta}\right), \tag{4.7}$$

$$C_{f,3} = -2\int_0^1 \left(1-\frac{y}{\delta}\right)^2 \left(\overline{I_x} + \frac{\partial \langle u\rangle}{\partial t}\right) \frac{\delta}{U_\infty^2}\,\mathrm{d}\left(\frac{y}{\delta}\right), \tag{4.8}$$

$$\overline{I_x} = \frac{\partial}{\partial x}\Big(\langle u\rangle^2\Big) + \frac{\partial}{\partial y}\Big(\langle u\rangle\,\langle v\rangle\Big) - \nu\frac{\partial^2\langle u\rangle}{\partial x^2} + \frac{\partial}{\partial x}\Big(\langle u'^2\rangle\Big). \tag{4.9}$$

The last two terms in the expression for $\overline{I_x}$ may be neglected in the framework of the turbulent boundary layer hypotheses, leading to the approximate relation:

$$\overline{I_x} = \frac{\partial}{\partial x}\Big(\langle u\rangle^2\Big) + \frac{\partial}{\partial y}\Big(\langle u\rangle\,\langle v\rangle\Big). \tag{4.10}$$

The FIK identity (4.5) is classically interpreted as a decomposition of mean friction according to the physical mechanisms of its generation. The first term $C_{f,1}$ is sometimes called the laminar contribution because of its similarity to laminar friction formulae. The second term $C_{f,2}$ is the turbulent contribution to the mean friction through the weighted integral of the Reynolds shear stress. It indicates that turbulent fluctuations at any height in the boundary layer may contribute to the mean friction, all the more as they get closer to the wall. The last term $C_{f,3}$ is related to the spatial heterogeneity of the boundary layer.

In the case of a steady channel flow, the FIK identity is similar, but $C_{f,3}$ vanishes because of the spatial homogeneity of the parallel flow. Also, the first term $C_{f,1}$ is equal to the friction coefficient C_f for a laminar flow with the same Reynolds number based on the bulk velocity and the channel width, as emphasized in Fukagata *et al.* (2002). This implies that $C_{f,2}$ represents the extra skin friction encountered for a given Reynolds number because of the turbulent fluctuations in comparison with the laminar case. The turbulent mean friction generation for a channel flow is thus fully characterized by the weighted Reynolds shear stress profile.

In the case of the spatially developing flat-plate boundary layer, the relation is less obvious, because $C_{f,3}$ is non-zero and cannot be easily related to its laminar counterpart. To make comparisons with the reference case of the laminar boundary layer, for which $C_{f,2,lam} = 0$, the Blasius self-similar solution of the laminar incompressible boundary layer equations with no pressure gradient detailed in Schlichting (1968) can be used. With x denoting the distance from the origin of the laminar boundary layer and $Re_x = xU_\infty/\nu$, it can be shown that:

$$C_{f,lam} = \frac{0.664}{\sqrt{Re_x}}, \quad C_{f,1,lam} = \frac{0.529}{\sqrt{Re_x}}, \quad C_{f,2,lam} = 0, \quad C_{f,3,lam} = \frac{0.135}{\sqrt{Re_x}}. \tag{4.11}$$

It is interest that the ratios of the FIK terms $C_{f,i,lam}$ to the total $C_{f,lam}$ do not depend on the Reynolds number for the self-similar laminar boundary layer:

$$C_{f,1,lam} = 0.79604C_{f,lam}, \quad C_{f,2,lam} = 0, \quad C_{f,3,lam} = 0.20396C_{f,lam}. \tag{4.12}$$

A Reynolds number definition for which the laminar $C_{f,1,lam}$ and $C_{f,3,lam}$ terms and their turbulent counterparts would coincide (in a similar way to the channel flow case with the Reynolds number based on bulk velocity and channel width) was sought with no success. Instead, the behaviour of the FIK terms $C_{f,1}$, $C_{f,2}$ and $C_{f,3}$ with respect to the Reynolds number is studied in the next subsection in order to identify potential parallels between the laminar and turbulent cases. The results suggest two reasons why, when focusing on $C_{f,2}$ alone, the study of turbulent friction generation at high Reynolds numbers does not seem to miss any major friction generation mechanism that could be represented by either $C_{f,1}$ or $C_{f,3}$.

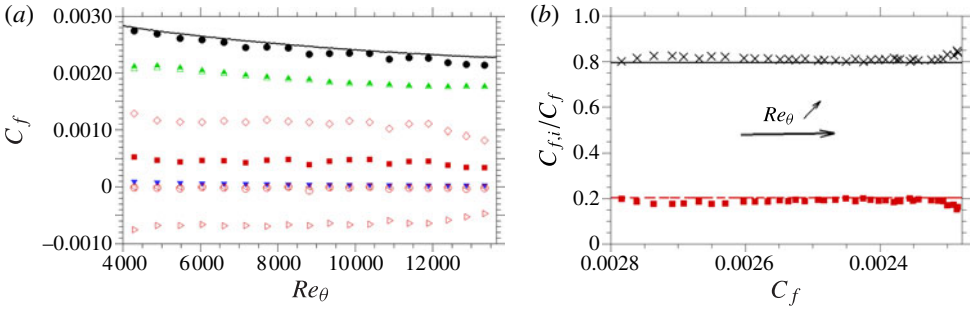

FIGURE 13. (Colour online) (*a*) Streamwise evolution of the FIK terms $C_{f,i}$ as a function of Re_θ. ——, C_f from computed wall shear stress; ▼, $C_{f,1}$; △, $C_{f,2}$, resolved part only; ▲, $C_{f,2}$, total (modelled and resolved parts); ■, $C_{f,3}$; ◊, $C_{f,3}$, contribution of $\partial/\partial x(\langle u\rangle^2)$; ▷, $C_{f,3}$, contribution of $\partial/\partial y(\langle u\rangle\langle v\rangle)$; ◁, $C_{f,3}$, contribution of $-\nu\partial^2\langle u\rangle/\partial x^2$; ∘, $C_{f,3}$, contribution of $\partial/\partial x(\langle u'^2\rangle)$; •, $C_{f,1}+C_{f,2}+C_{f,3}$. (*b*) Streamwise evolution of the relative FIK terms $C_{f,i}/C_f$. $(C_{f,1}+C_{f,2})/C_f$: ×, present; ——, laminar solution (Blasius (4.12)) for the same C_f. $C_{f,3}/C_f$: ■, present; – – –, laminar solution (Blasius (4.12)) for the same C_f. Note that the abscissa is reversed (decreasing C_f and increasing Re_θ).

4.2. *Evolution of the FIK identity in high-Reynolds-number flat-plate boundary layers*

The Reynolds-number dependence of the FIK terms $C_{f,1}$, $C_{f,2}$ and $C_{f,3}$ computed in the present simulation is depicted in figure 13(*a*). It is important to note that the contribution of the modelled Reynolds shear stress to $C_{f,2}$ can be neglected, as demonstrated by the very close values for the resolved and total $C_{f,2}$ shown in the same figure. The modelled part amounts to less than 2 % of the total C_f at the considered Reynolds numbers.

First of all, the total friction coefficient computed by numerical integration of the integral terms of the FIK identity is compared with the same coefficient directly estimated from the wall-normal gradient of streamwise velocity at the wall. Excellent agreement is found between the two methods. It should be noted that the first term $C_{f,1}$ is much smaller than the other two. It may also be checked in figure 13 that two of the four terms contributing to $C_{f,2}$ actually are negligible, as implied by the boundary layer hypothesis (see (4.10)). Furthermore, over the Reynolds number range covered, the second term $C_{f,2}$ is approximately four times greater than the third one $C_{f,3}$. This suggests that most of the friction drag is associated with the second term $C_{f,2}$, on which the analysis of friction generation may consequently focus.

However, this would imply that $C_{f,3}$ is merely neglected, even though it amounts to approximately 20 % of the total C_f, as can be seen on figure 13(*b*). In addition, contrary to the channel flow case, the first and third terms $C_{f,1}$ and $C_{f,3}$ depend on the turbulent fluctuations. Indeed, even though they formally involve only the mean value of velocity and not its second-order statistical moments, the mean velocity profile itself depends on the Reynolds shear stress. This means that evaluating the impact of a given type of turbulent coherent structures on mean friction should cover both its impact on $C_{f,2}$ but also on the other two FIK terms. Nevertheless, in the following some reasons are shown for why the study of the contribution of the turbulent fluctuations to $C_{f,2}$ only appears to be sufficient for an accurate description of turbulent friction generation.

Indeed, a particular feature of the evolution of the FIK terms with the Reynolds number is shown in figure 13(*b*). This figure presents the ratio $C_{f,3}/C_f$ for the

present simulation, compared to the value it has in the laminar case (see (4.12)). It is demonstrated in the previous subsection that in the case of a laminar boundary layer, the ratios $C_{f,1}/C_f$ and $C_{f,3}/C_f$ remain constant whatever the Reynolds number. Since computing such quantities emphasizes the value of C_f, C_f is used as the x-axis variable, but in reversed scale so that the Reynolds number is increasing towards the right-hand side.

The first striking feature in figure 13(*b*) is the relatively constant value of the ratio $C_{f,3}/C_f$ over the considered Reynolds number range for the present turbulent boundary layer. A second striking fact is the very close values taken by this ratio in the laminar and in the turbulent case. It will be shown in the next subsection that theoretical considerations tend to predict that the turbulent value of $C_{f,3}/C_f$ is asymptotically constant for high Reynolds numbers. It will also be shown how the laminar case and the high-Reynolds-number turbulent case end up with a very similar value of $C_{f,3}/C_f$, even though there is no obvious theoretical reason for the values to be equal.

Since $C_{f,3}/C_f$ is found to be almost constant and close to the laminar case value, the sum of the other two FIK terms $(C_{f,1}+C_{f,2})/C_f = 1 - C_{f,3}/C_f$ has to follow the same trend, which can be seen in figure 13(*b*). However, even though $(C_{f,1}+C_{f,2})/C_f$ is almost constant in the high-Reynolds-number turbulent case and has a value close to its laminar counterpart, it involves a very different distribution of the contributing terms $C_{f,1}$ and $C_{f,2}$: in the turbulent case, $(C_{f,1}+C_{f,2})/C_f \approx C_{f,2}/C_f$, while in the laminar case $(C_{f,1}+C_{f,2})/C_f = C_{f,1}/C_f$.

These observations suggest a new way of reasoning, presented in the following, that supports the focus on the contribution of the high-Reynolds-number turbulent coherent structures only to $C_{f,2}$.

A Reynolds number Re_α is first defined, based on the characteristic length $\alpha = \delta/(1-\delta_1/\delta)$, so that:

$$Re_\alpha = \frac{Re_\delta}{1-\delta_1/\delta}. \tag{4.13}$$

This definition is motivated by the resulting relation:

$$C_{f,1} = \frac{4}{Re_\alpha}. \tag{4.14}$$

Since the ratio δ_1/δ is constant in the laminar case and varies slowly in the turbulent case, the behaviour of Re_α is similar to the more common Reynolds number Re_δ. The evolution of Re_θ with Re_α in the present turbulent simulation is presented in figure 14(*b*), confirming that this newly defined Reynolds number does increase with the more usual Reynolds number. The laminar and turbulent C_f are plotted as a function of Re_α in figure 14(*a*). The dependence of the laminar C_f on the Reynolds number Re_α is deduced from equations (4.12) and (4.14):

$$C_{f,lam} = \frac{5.025}{Re_\alpha}. \tag{4.15}$$

It is now shown that the acknowledged extra skin friction of a turbulent boundary layer compared to a laminar boundary layer with the same Reynolds number can be attributed to the FIK term $C_{f,2}$ alone, making irrelevant the study of the impact of the turbulent fluctuations on $C_{f,1}$ and $C_{f,3}$. More specifically, it is shown in the following that if the ratio $C_{f,3}/C_f$ is assumed to have the same value in the laminar case as in the high-Reynolds-number turbulent cases, then the higher value of C_f in

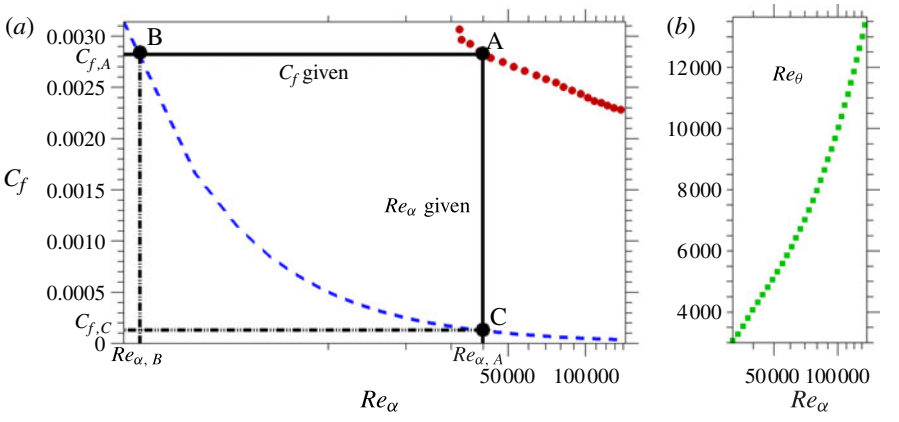

FIGURE 14. (Colour online) (*a*) Friction coefficient C_f as a function of the Reynolds number Re_α defined by (4.13).– – –: laminar case $C_f = 5.025/Re_\alpha$; •, present turbulent boundary layer simulation. (*b*) Reynolds number based on the momentum thickness Re_θ plotted in the turbulent case as a function of Re_α.

the turbulent case compared to the laminar case at the same Re_α only results from the strictly positive value of $C_{f,2}$ in the turbulent case compared to its zero value in the laminar case. This emphasizes the key role of the FIK term $C_{f,2}$ in the turbulent friction generation and justifies that only this term need be studied to characterize turbulent friction.

Returning to figure 14(*a*), it has to be shown that point A of the turbulent case, characterized by the Reynolds number $Re_{\alpha,A}$ and the friction coefficient $C_{f,A}$, has a greater C_f than point C which represents the laminar case at the same $Re_\alpha = Re_{\alpha,A}$ with a friction coefficient $C_{f,C}$, from only two assumptions:

(i) the ratio $C_{f,3}/C_f$ for point A has the same value as the laminar case value;
(ii) $C_{f,2} > 0$ in A and $C_{f,2} = 0$ in the laminar case, which results from the well-known properties of the Reynolds shear stress sign in the laminar and turbulent boundary layers.

In an intermediate step, the laminar case with the same C_f (point B) instead of the same Re_α is considered. The motivation for considering a given C_f comes from the observed property of the ratios $C_{f,3}/C_f$ and $(C_{f,1} + C_{f,2})/C_f$ remaining constant, which suggests using a reference C_f. For a given $C_f = C_{f,A}$, it has been shown that the sum $C_{f,1} + C_{f,2}$ has very close values in the laminar and in the high-Reynolds-number turbulent cases. However, $C_{f,2}$ is zero in the laminar case and strictly positive in the turbulent case. This implies that for a given $C_f = C_{f,A}$, the Reynolds number $Re_{\alpha,B}$ in the laminar case is smaller than the Reynolds number $Re_{\alpha,A}$ in the turbulent case, because of the relation:

$$C_{f,1} + C_{f,2} = \frac{4}{Re_\alpha} + C_{f,2} \approx \text{constant} \quad \text{for a given } C_f. \tag{4.16}$$

This implies that for a strictly positive $C_{f,2}$ caused by the turbulent fluctuations, point A is located to the right of point B in figure 14(*a*) ($Re_{\alpha,A} > Re_{\alpha,B}$). Because of the behaviour of C_f with Re_α in the laminar case, this clearly implies that point A is located above the laminar case curve. As a consequence, for a given Reynolds number

$Re_\alpha = Re_{\alpha,A}$, the turbulent case point A is located above the laminar case point C, i.e. the turbulent friction coefficient $C_{f,A}$ is greater than its laminar counterpart $C_{f,C}$. The previous reasoning has shown that the level of $C_{f,2}$ at a given C_f is directly related to the difference between the turbulent and laminar C_f at a given Re_α, as long as the ratio $C_{f,3}/C_f$ may be assumed independent of the Reynolds number in the turbulent case and close to the laminar case value.

The impact of $C_{f,2}$ in the turbulent case at high Reynolds numbers, where it is much greater than $C_{f,1}$ ($C_{f,1}$ is less than 3 % of the total C_f over the considered Reynolds number range), can be seen as simply determining which small amount is left for $C_{f,1}$ at the considered value of C_f, thus determining the value of Re_α. Consequently, the study of mean friction generation can focus on $C_{f,2}$, just as in the case of the channel flow. This can alternatively be seen from the following relation:

$$\begin{aligned} 1 &= \frac{C_{f,1}}{C_f} + \frac{C_{f,2}}{C_f} + \frac{C_{f,3}}{C_f} \\ &= \frac{4}{C_f Re_\alpha} + \frac{C_{f,2}}{C_f} + \frac{C_{f,3}}{C_f} \end{aligned} \tag{4.17}$$

which, if $C_{f,3}/C_f$ is assumed to be approximately constant in the high-Reynolds-number turbulent range, leads to $4/(C_f Re_\alpha) + C_{f,2}/C_f \approx$constant for any high Reynolds number. Since C_f does not decay as fast as $1/Re_\alpha$ in the turbulent case (because a $1/Re_\alpha$ decay corresponds to the laminar case), $4/(C_f Re_\alpha)$ decreases with the Reynolds number. Consequently, in the turbulent boundary layer, $C_{f,1}/C_f$ decreases towards zero with the Reynolds number, whereas $C_{f,2}/C_f$ increases so that $(C_{f,1} + C_{f,2})/C_f$ stays approximately constant, just as $C_{f,3}/C_f$. The increase of the relative contribution of $C_{f,2}$ to C_f can finally be seen as the main result of the evolution of the turbulent coherent structures with increasing Reynolds numbers.

One last alternative point of view resorts to the ratio $C_f/(C_{f,1} + C_{f,2})$, which is constant when $C_{f,3}/C_f$ is assumed to be constant. For a given Reynolds number Re_α, the laminar and the turbulent boundary layers have the same $C_{f,1}$ (by definition of this Reynolds number, see (4.14)). The sum $C_{f,1} + C_{f,2}$ is greater in the turbulent case (where $C_{f,2} > 0$) than in the laminar case (where $C_{f,2} = 0$). The total C_f is then obtained from the product of the sum $C_{f,1} + C_{f,2}$ times the ratio $C_f/(C_{f,1} + C_{f,2})$, which is assumed to have the same value in the laminar and turbulent cases. By noting that for a given Re_α,

$$C_{f,lam} = \frac{C_f}{C_{f,1} + C_{f,2}} \left(C_{f,1} + 0\right) \tag{4.18}$$

and

$$C_{f,turb} = \frac{C_f}{C_{f,1} + C_{f,2}} \left(C_{f,1} + C_{f,2}\right), \tag{4.19}$$

where $C_f/(C_{f,1} + C_{f,2})$ is assumed to have the same constant value in the laminar and turbulent case, one can conclude that the extra drag of the turbulent boundary layer compared to its laminar counterpart of same Re_α is equal to

$$C_{f,turb} - C_{f,lam} = \frac{C_f}{C_{f,1} + C_{f,2}} C_{f,2} \tag{4.20}$$

which is directly proportional to the FIK term $C_{f,2}$ related to the weighted Reynolds shear stress profile.

It should however be noted that the above reasoning relies on the assumption that the ratio $C_{f,3}/C_f$ does not depend much on the turbulent structures present in the boundary layer. This has been suggested to be almost the case in the high-Reynolds-number range considered, but is not necessarily the case for other boundary layers, for instance the lower-Reynolds-number turbulent one, or an artificially forced turbulent boundary layer.

In particular, the values shown in Lee *et al.* (2013) of the FIK terms from a DNS of a turbulent boundary layer with and without wall heating tend to suggest that the value of $C_{f,3}/C_f$ might be higher at low to moderate Reynolds numbers ($Re_\theta = 1240$ to 2060) than in the laminar and high-Reynolds-number turbulent cases. The authors also suggest that the impact of wall heating on this ratio decreases with the Reynolds number. This leads to the hypothesis that the trend observed in the present simulation is valid only for asymptotically high Reynolds numbers, which is fully supported by the theoretical considerations of the next subsection.

4.3. *A possible explanation of the behaviour of $C_{f,3}/C_f$ based on outer layer self-similarity at high Reynolds numbers*

In this subsection, theoretical support is given for the observed trend of an approximately constant value of the ratio $C_{f,3}/C_f$ at high Reynolds numbers. It is also shown how the values in the turbulent and laminar cases can be close to each other. This last point is extremely confusing if considered from the classical point of view according to which the third FIK term $C_{f,3}$ is describing the spatial growth of the boundary layer, which is much faster in the turbulent case than in the laminar one.

The first step to draw parallels between these very different cases consists of rewriting $C_{f,3}$ in a different manner. Using the Reynolds-averaged Navier–Stokes streamwise momentum equation within the boundary layer hypotheses framework, this term can be rewritten, with no approximation, in terms of the profile of the wall-normal gradient of the total shear stress $\tau/\rho = \nu\partial\langle u\rangle/\partial y - \langle u'v'\rangle$ only:

$$C_{f,3} = -2\int_0^1 \left(1-\frac{y}{\delta}\right)^2 \frac{\partial(\tau/\rho)}{\partial y}\frac{\delta}{U_\infty^2}\,\mathrm{d}\left(\frac{y}{\delta}\right). \tag{4.21}$$

This induces a very different interpretation of this term compared to its usual description as the spatial heterogeneity term: $C_{f,3}$ also describes the total shear stress normal gradient profile. The relation between the two points of view simply relies on the streamwise momentum balance.

It is known that the total shear stress in a turbulent boundary layer is approximately constant in the inner layer. At the wall, the total stress is purely viscous. Away from the wall, the viscous part gradually decreases but a simultaneous increase of the Reynolds shear stress compensates for it so that the total shear stress is constant. Even further away from the wall, the logarithmic layer can be characterized by a constant Reynolds shear stress, and since the viscous stress is negligible in this region at high Reynolds numbers, the total shear stress is constant in that layer too. Consequently, one may assume that $\partial(\tau/\rho)/\partial y \approx 0$ from the wall to the outer edge of the logarithmic layer, meaning that the integral giving $C_{f,3}$ almost depends only on the outer layer.

The integral for $C_{f,3}$ is next rewritten in order to introduce the usual outer scaling and to isolate the total C_f:

$$C_{f,3} = -C_f\int_0^1 \left(1-\frac{y}{\delta}\right)^2 \frac{\partial\tau^+}{\partial(y/\delta)}\,\mathrm{d}\left(\frac{y}{\delta}\right), \tag{4.22}$$

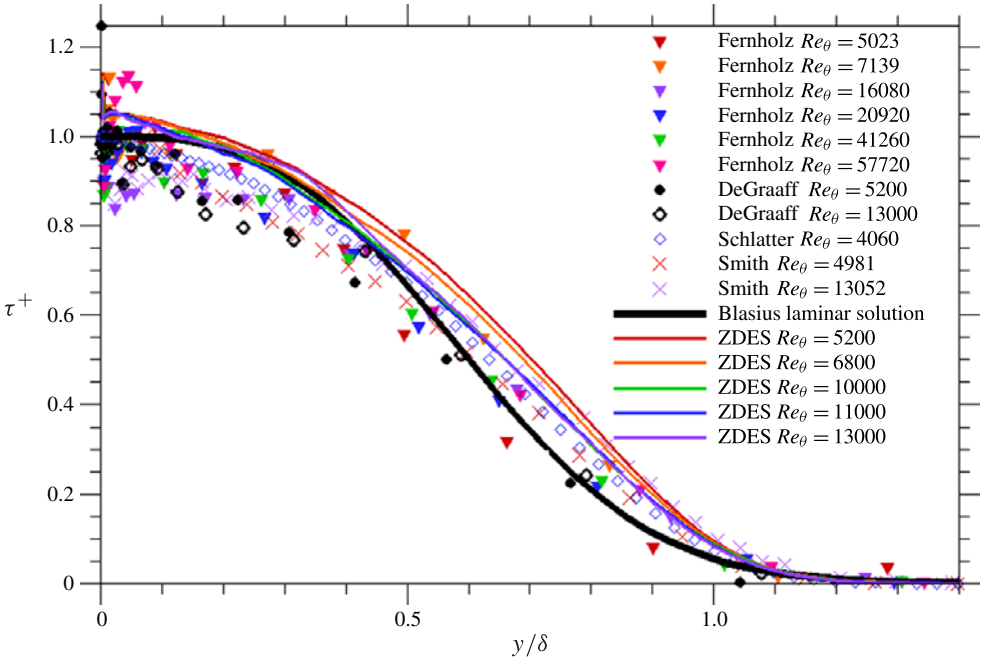

FIGURE 15. (Colour online) Normalized total shear stress $\tau^+ = \tau/\tau_w$. Data from the references given in the table 3.

where $\tau^+ = \tau/\tau_w$ is the total shear stress non-dimensionalized by the wall shear stress $\tau_w = \rho u_\tau^2$.

As already mentioned, the total shear stress varies significantly only in the outer layer of the turbulent boundary layer. Consequently, as shown by equation (4.22), the ratio $C_{f,3}/C_f$ is independent of the Reynolds number if the profile in the outer layer of the non-dimensionalized total shear stress $\tau^+(y/\delta)$ does not depend on the Reynolds number. This can be seen as a self-similarity property of the outer layer.

Figure 15 investigates whether such a self-similarity exists in high-Reynolds-number turbulent boundary layers. Experimental data, DNS simulations and the data from the present simulation, altogether covering a very wide range of high Reynolds numbers (approximately $Re_\theta = 4000$ to $Re_\theta = 50\,000$), are presented. Apart from experimental and numerical scatter, it seems that all the profiles collapse, as had already been suggested in figure 25 of DeGraaff & Eaton (2000). This strongly supports the existence of a self-similar total shear stress profile $\tau^+(y/\delta)$ in the outer layer. As a consequence of this possible self-similarity, the above equations show that the ratio $C_{f,3}/C_f$ is approximately constant for high Reynolds numbers.

One may find it surprising that the total shear stress profile could be independent of the Reynolds number, although it includes the viscous stress contribution, which explicitly depends on it. However, the above formulation of $C_{f,3}$ can be expanded:

$$C_{f,3} = -C_f \int_0^1 \left(1 - \frac{y}{\delta}\right)^2 \frac{\partial}{\partial(y/\delta)} \left(\frac{1}{Re_\tau} \frac{\partial \langle u \rangle^+}{\partial y/\delta} - \langle u'v' \rangle^+ \right) \mathrm{d}\left(\frac{y}{\delta}\right). \tag{4.23}$$

The $1/Re_\tau$ factor emphasizes the dependence of the viscous stress on the Reynolds number, but also shows that in the limit of high Reynolds numbers, the viscous

stress in the outer layer becomes very small compared to the Reynolds shear stress. This suggests that the self-similarity of the total shear stress in the outer layer simply results from the self-similarity of the Reynolds shear stress $-\langle u'v'\rangle^+(y/\delta)$ in the outer layer, which does not depend explicitly on the Reynolds number. The self-similarity of the latter profile does not seem impossible from a theoretical point of view, because turbulence tends to adapt its dissipative scales so that the amount of dissipation matches the large-scale energy production in a process where the dependence on the Reynolds number may disappear. One well-known example is the friction coefficient over a sand-roughened flat plate in fully rough flow conditions, which depends only on the relative roughness k_s/x and not on the Reynolds number. The self-similarity of $-\langle u'v'\rangle^+(y/\delta)$ was already suggested in DeGraaff & Eaton (2000). Furthermore, the mean streamwise velocity profile can be satisfactorily described by a self-similar outer layer law, given for instance by Coles' law of the wake (Coles 1956), and since the Reynolds shear stress is related to the mean velocity by the streamwise momentum equation, it makes sense that it is self-similar in the outer layer as well.

The above reasoning gives some insight into why the ratio $C_{f,3}/C_f$ seems to tend to a constant value in the limit of high Reynolds numbers for the turbulent boundary layer. However, it does not explain why this value is very close to its laminar counterpart. The way that the integral for $C_{f,3}$ has been reformulated is still valid in the laminar case. This implies that to understand the value of $C_{f,3,lam}/C_{f,lam}$, one could consider the profile of the total shear stress non-dimensionalized in the same way as in the turbulent case. Using the Blasius solution presented in Schlichting (1968), with the similarity parameter $\eta = y\sqrt{U_\infty/(\nu x)}$ and the streamwise velocity profile $\overline{u}/U_\infty = f'(\eta)$, the total shear stress non-dimensionalized by the wall shear stress is:

$$\tau^+ = \frac{\mu\dfrac{\partial\langle u\rangle}{\partial y}(y)}{\mu\dfrac{\partial\langle u\rangle}{\partial y}(y=0)} = \frac{f''(\eta)}{f''(0)}, \tag{4.24}$$

where the values of the function $f''(\eta)$ can be found in Schlichting (1968) and $\eta \approx 4.92\,y/\delta$.

Using these equations, the laminar profile $\tau^+(y/\delta)$ is plotted in figure 15 together with the data for turbulent boundary layers. Even though the laminar total shear stress profile is slightly different from the profile which the turbulent case seems to tend to at infinitely high Reynolds numbers, the two profiles are surprisingly close to each other. No physical explanation could be found for this feature, but it is believed that the absence of a major difference between the profiles results in the close values taken by $C_{f,3}/C_f$ in both cases.

From this subsection it may be concluded that there are some theoretical grounds supporting the assumed constant value of the ratio $C_{f,3}/C_f$ in the high-Reynolds-number turbulent case and the very similar value this ratio takes in the laminar case. As explained in the previous subsection, this motivates the focus on the second FIK term $C_{f,2}$ alone, and consequently on the Reynolds shear stress only, to study how the coherent structures observed in high-Reynolds-number flat-plate turbulent boundary layers contribute to mean wall shear stress.

5. Scale decomposition of mean wall shear stress

As detailed in the previous section, the study of the contribution of the turbulent coherent structures to mean wall shear stress can focus on the second term $C_{f,2}$ of

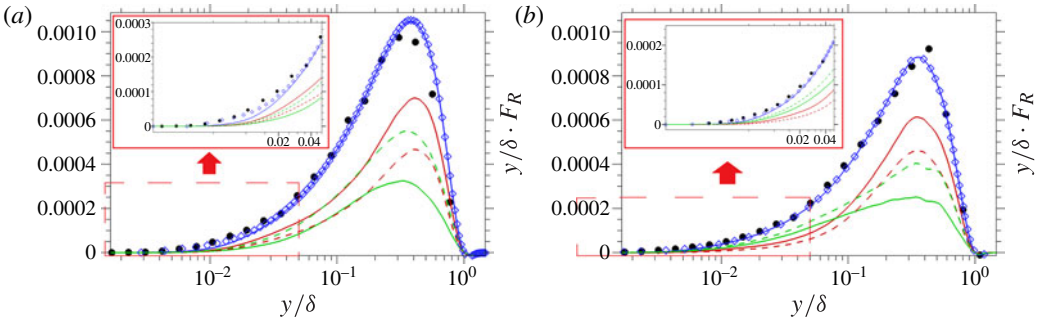

FIGURE 16. (Colour online) Contribution of the large and small scales to $(y/\delta)F_R$ (from (5.2)) at $Re_\theta = 5200$ (*a*) and $Re_\theta = 13\,000$ (*b*). •, Exp. DeGraaff & Eaton (2000); blue solid line resolved signal (present ZDES); green solid line $\lambda_x < \delta$; red solid line $\lambda_x \geqslant \delta$; green dashed line, $\lambda_x < 2\delta$; red dashed line, $\lambda_x \geqslant 2\delta$; ⋄, total $(y/\delta)F_R$ (resolved and modelled parts, present ZDES).

the FIK identity (4.5). This term may be rewritten as:

$$C_{f,2} = \int_0^1 F_R \, \mathrm{d}\left(\frac{y}{\delta}\right), \tag{5.1}$$

where F_R represents the weighted contribution of the Reynolds shear stress to mean friction as described by the FIK identity:

$$F_R = -4\frac{\langle u'v' \rangle}{U_\infty^2}\left(1 - \frac{y}{\delta}\right). \tag{5.2}$$

As mentioned before, to the authors' knowledge the FIK identity provides the only way of describing the turbulent contribution to mean wall shear stress by a quantity, F_R, whose integral over the wall distance amounts to turbulent friction, which motivated the framework of the present analysis.

If the term F_R is multiplied by y/δ, the contribution to $C_{f,2}$ is proportional to the area below the $(y/\delta)F_R$ curve as a function of y/δ plotted in logarithmic scale. One such plot is shown in figure 16, where the present simulation is compared with experimental data for two different Reynolds numbers. It can be seen that the contribution to $C_{f,2}$ is very well captured by the simulation. It may also be noted that the outer layer represents the most significant part of the contribution to $C_{f,2}$, which was the motivation for the refinement of the mesh in the outer layer at the expense of the full resolution of the inner layer (as discussed in § 2). This figure also shows the reconstructed total $(y/\delta)F_R$, where the resolved and modelled Reynolds shear stresses have been added. The modelled part is negligible in the areas where $(y/\delta)F_R$ takes significant values, which implies that the resolved fluctuations can be used directly for the analysis in the framework of the FIK identity. In particular, the most significant contribution is located in the outer layer, where it has been shown that the streamwise velocity spectrum matches well experimental data, so that the present simulation is expected to provide a good resolution of the contribution to $C_{f,2}$. A scale decomposition is also shown in this figure and will be discussed in § 5.2.

In the following, the term F_R is decomposed according to the length scale of the contributing turbulent fluctuations. This involves a spectral analysis of F_R, presented

in the next subsection. The spectra can then be integrated over the length scale and over the distance to the wall to assess the local and global contribution of the larger scales to skin friction.

5.1. *Spectral analysis of the Reynolds shear stress*

Performing a spectral analysis of F_R is equivalent to computing the spectrum of the Reynolds shear stress at a given distance y from the wall, because it is the only statistical moment present in the definition of F_R (5.2). The spectral analysis is made in the same way as for the streamwise velocity fluctuations presented in § 3.4. This means that the two spectra can be compared, for instance to assess whether the large-scale structures that have been visualized and emphasized by the streamwise velocity spectra contribute to mean wall shear stress. Consequently, the convection velocity used to reconstruct a spatial spectrum from the time signal by Taylor's frozen turbulence hypothesis is the Reynolds-averaged streamwise velocity, just as in § 3.4. It should be noted that as emphasized previously, this procedure may lead to some underestimation of the size of the largest structures near the wall. As a consequence, the contribution of the largest scales to mean skin friction could be underestimated. Some details are given here on the way the spectral analysis of the Reynolds shear stress is performed. The signals available from the simulation are the time signals of the streamwise and wall-normal velocity $u(t)$ and $v(t)$ at the considered x and y location. The cross-correlation of these signals is defined as:

$$R_{12}(\tau) = \left\langle u'(t)v'(t+\tau)\right\rangle . \tag{5.3}$$

The cross-power spectral density of u' and v' is the Fourier transform of the cross-correlation:

$$S_{u'v'}(f) = \int_{-\infty}^{\infty} R_{12}(\tau)\mathrm{e}^{-2\mathrm{i}\pi f\tau}\,\mathrm{d}\tau. \tag{5.4}$$

The cross-correlation can be expressed as the inverse Fourier transform of the cross-power spectral density:

$$R_{12}(\tau) = \int_{-\infty}^{\infty} S_{u'v'}(f)\mathrm{e}^{2\mathrm{i}\pi f\tau}\,\mathrm{d}f. \tag{5.5}$$

By definition $R_{12}(\tau = 0) = \langle u'v'\rangle$, which gives:

$$\left\langle u'v'\right\rangle = \int_{-\infty}^{\infty} S_{u'v'}(f)\,\mathrm{d}f. \tag{5.6}$$

Moreover, it can be seen from (5.4) that $S_{u'v'}(f)$ and $S_{u'v'}(-f)$ are complex conjugates. This leads to the final formulation of $\langle u'v'\rangle$, where Re denotes the real part:

$$\begin{aligned}\left\langle u'v'\right\rangle &= \int_{-\infty}^{\infty} S_{u'v'}(f)\,\mathrm{d}f \\ &= \int_{0}^{\infty} \left(S_{u'v'}(-f) + S_{u'v'}(f)\right)\,\mathrm{d}f \\ &= \int_{0}^{\infty} 2\mathrm{Re}(S_{u'v'}(f))\,\mathrm{d}f.\end{aligned} \tag{5.7}$$

The premultiplied spatial co-spectrum (i.e. the real part of the premultiplied one-sided cross-power spectral density) is estimated from Taylor's hypothesis with the local convection velocity U_c, leading to the following relations:

$$k_x = \frac{2\pi f}{U_c}, \tag{5.8}$$

$$\frac{\langle u'v' \rangle}{u_\tau^2} = \int_0^\infty \frac{\Phi_{uv}(k_x)}{u_\tau^2}\,\mathrm{d}k_x, \tag{5.9}$$

$$k_x \Phi_{uv}(k_x) = 2f\mathrm{Re}(S_{u'v'}(f)). \tag{5.10}$$

The contribution of the wavenumber band $[k_{x,1}, k_{x,2}]$ to $\langle u'v' \rangle$ can be computed by truncating the integral:

$$\frac{\langle u'v' \rangle_{[k_{x,1},k_{x,2}]}}{u_\tau^2} = \int_{k_{x,1}}^{k_{x,2}} \frac{\Phi_{uv}}{u_\tau^2}\,\mathrm{d}k_x. \tag{5.11}$$

The premultiplied spectrum $k_x\Phi_{uv}$, when plotted versus the wavenumber k_x in logarithmic scale, shows the contribution of each wavenumber band proportionally to the area located below the curve:

$$\frac{\langle u'v' \rangle}{u_\tau^2} = \int_{-\infty}^{\infty} \frac{k_x\Phi_{uv}}{u_\tau^2}\,\mathrm{d}(\ln(k_x)). \tag{5.12}$$

Returning to the FIK identity, the co-spectrum Φ_{F_R} of F_R defined by (5.2) is given by:

$$\Phi_{F_R} = -4\frac{\Phi_{uv}}{U_\infty^2}\left(1 - \frac{y}{\delta}\right), \tag{5.13}$$

so that

$$F_R = \int_{-\infty}^{\infty} k_x\Phi_{F_R}\,\mathrm{d}(\ln(k_x)) \tag{5.14}$$

and finally:

$$C_{f,2} = \int_{-\infty}^{0}\int_{-\infty}^{\infty} k_x\frac{y}{\delta}\Phi_{F_R}\mathrm{d}(\ln(k_x))\,\mathrm{d}\left(\ln\left(\frac{y}{\delta}\right)\right). \tag{5.15}$$

Plotting $k_x(y/\delta)\Phi_{F_R}$ in the (λ_x, y) plane with logarithmic scales for both the wall distance and the streamwise wavelength thus provides a map of the local contribution of a given scale at a given height above the wall to mean wall shear stress. The contribution is proportional to the volume located below the $k_x(y/\delta)\Phi_{F_R}$ surface. One such plot is shown in figure 17 for the present simulation, at two Reynolds numbers $Re_\theta = 5200$ and $Re_\theta = 13\,000$. The power spectral density of the streamwise velocity fluctuations is also shown as dashed lines so that a comparison is possible.

The most striking feature from figure 17 is that the inner energy site that could be seen on the streamwise velocity spectra contributes very little to $C_{f,2}$, to such an extent that the inner site cannot even be seen in the contours of $k_x(y/\delta)\Phi_{F_R}$. This results from the weighting of the FIK identity and from the premultiplication used for the plot in logarithmic scale. On the contrary, the outer site, corresponding to the larger scales located in the outer layer, gives the main contribution to $C_{f,2}$, with a very good match between the spectra of the streamwise velocity and the contribution to skin

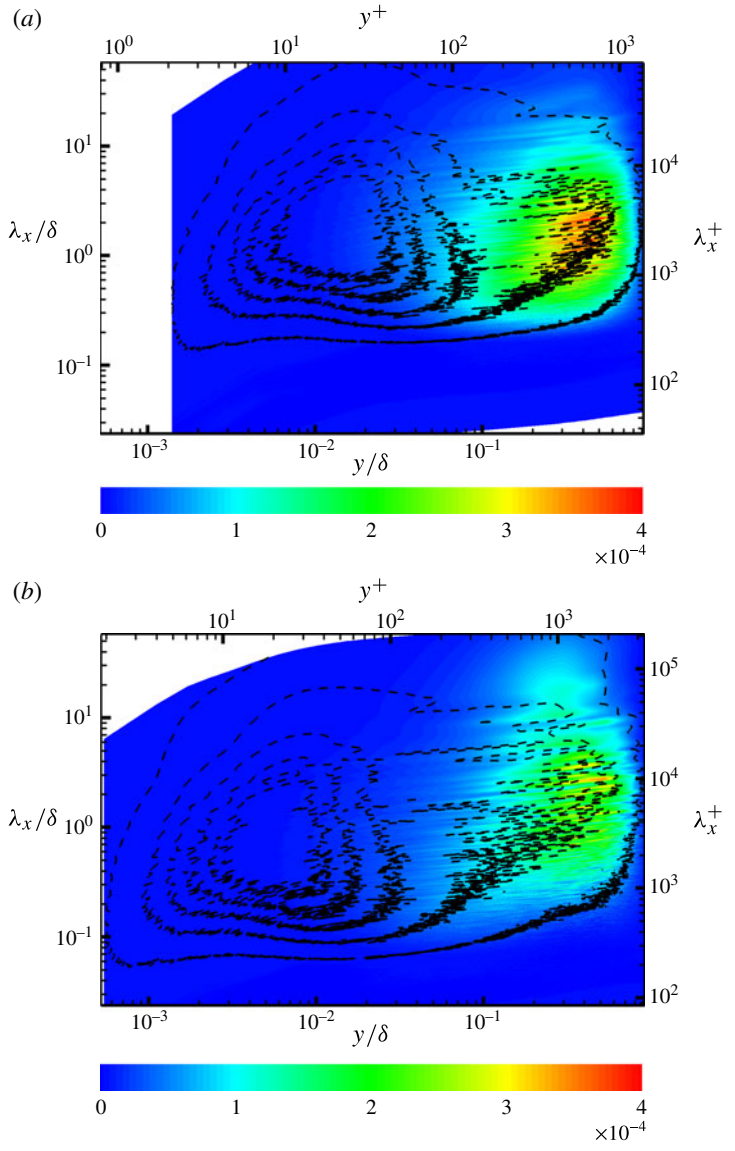

FIGURE 17. (Colour online) Premultiplied local contribution $k_x(y/\delta)\Phi_{F_R}$ to mean wall shear stress (5.15) at $Re_\theta = 5200$ (*a*) and $Re_\theta = 13\,000$ (*b*). Coloured map: present simulation. Dashed lines: isocontours from the streamwise velocity spectrum (present simulation) shown in figure 11.

friction in the outer layer. It should of course be mentioned that this decomposition of the mean friction generation relies on a mathematical transformation of the governing equations according to the method first introduced by Fukagata *et al.* (2002), and not on a physical reasoning. Consequently, the map of the contributions shown in this figure should not be interpreted as a map of the root causes of friction generation, as for instance some inner layer phenomena may be necessary for the outer layer Reynolds-shear-stress-carrying structures to appear.

The Reynolds number dependence of the site of the main contribution to $C_{f,2}$ is weak in figure 17, except for the fact that the overall level is lower because the total C_f is smaller at higher Reynolds numbers. Indeed, outer scales have been chosen, which are well-suited for the use of the FIK identity because of the way it is formulated, but which are also well-suited to describe phenomena taking place in the outer layer. This result is fully consistent with the possible self-similarity of the Reynolds shear stress profile in the outer layer evoked in the previous section. One may note however that at the higher Reynolds number, the contribution to $C_{f,2}$ seems to involve larger scales, even though its integral value over all scales might be unchanged in the outer layer. Figure 17 also suggests that the very large-scale motions that have been visualized in § 3 and suggested by the streamwise velocity spectra in § 3.4 might also carry a significant contribution to mean wall shear stress, with a non-negligible contribution of wavelengths larger than 10δ at the higher Reynolds number presented. In the next subsection, several estimations of the scale decomposition of mean wall shear stress are made.

5.2. *Assessment of large-scale contribution to skin friction*

The contribution to $C_{f,2}$ of the large and small scales can be evaluated from the map presented in figure 17 by integrating over the wavelength. This is quite similar to the discussion on the streamwise velocity spectrum, for which a cut-off wavelength has been chosen. Figure 16 presents the decomposition of the premultiplied contribution $(y/\delta)F_R$ (see (5.2)) to $C_{f,2}$ with the same two cut-off wavelengths $\lambda_c = \delta$ and 2δ as before. As had already been emphasized, at the lower Reynolds number, small inner-scaled wavelengths are not well separated from the larger outer-scaled wavelengths, which makes the decomposition very sensitive to the cut-off wavelength. This sensitivity is weaker at higher Reynolds numbers. The comparison with the similar decomposition performed in figure 12 reveals that towards high Reynolds numbers, even though the larger wavelengths significantly contribute to the streamwise turbulence intensity in the inner layer, their contribution to $C_{f,2}$ becomes relatively small in the inner layer compared to the contribution of the smaller scales. This suggests that the large-scale structures that can be seen contribute much to mean wall shear stress by their outer layer activity, but their footprint in the inner layer, which is significant in terms of streamwise fluctuations, does not contribute significantly to mean wall shear stress. This is not the case at the lower Reynolds number considered, suggesting that the feet of the very large-scale motions may be seen as inactive in the sense of Townsend (Townsend 1976) only in the limit of asymptotically high Reynolds numbers. Conversely, the largest scales ($\lambda_x \geqslant 2\delta$) make an increasingly important contribution to the Reynolds shear stress in the outer layer.

It is then possible to assess the overall contribution of the large and small scales to $C_{f,2}$ by integrating the previous profiles over y. The full decomposition of C_f according to the FIK identity and with two different cut-off wavelengths is presented in figure 18 for the two considered Reynolds numbers. The relative share of $C_{f,1}$ and $C_{f,3}$ has already been discussed in § 4. It can be seen that the largest scales contribute significantly to the overall C_f. At $Re_\theta = 5200$, depending on the cut-off wavelength, the contribution of the largest scales to $C_{f,2}$ ranges from 65 % ($\lambda_c = \delta$) to 44 % ($\lambda_c = 2\delta$). This becomes 63 % to 47 % at $Re_\theta = 13\,000$ with the same cut-off wavelengths. Let us be reminded that these percentages are related to the second term of the FIK identity $C_{f,2}$ only, whereas the values given in figure 18 refer to the total C_f. It should be noted that the relative contribution of the large scales increases

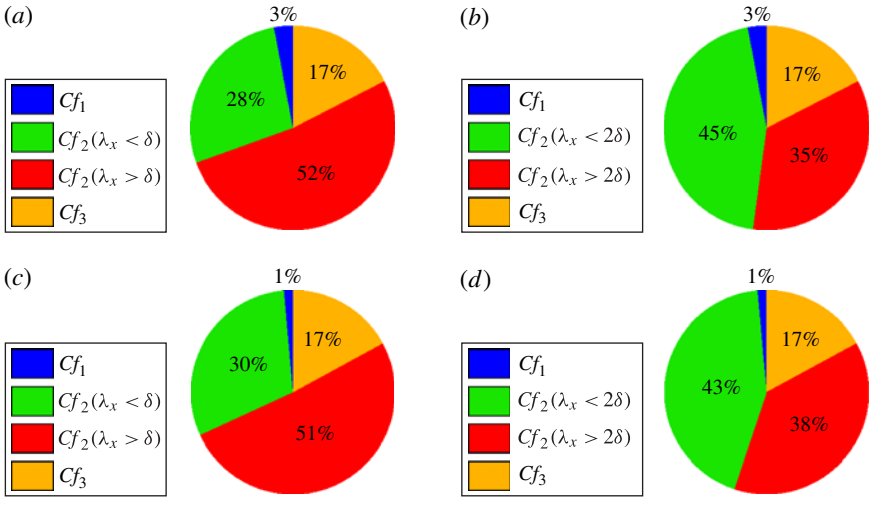

FIGURE 18. (Colour online) Decomposition of C_f (present simulation) according to the FIK identity with scale decomposition of $C_{f,2}$ at cut-off wavelength $\lambda_x = \lambda_c$, (*a*) $Re_\theta = 5200$, $\lambda_c = \delta$, (*b*) $Re_\theta = 5200$, $\lambda_c = 2\delta$, (*c*) $Re_\theta = 13\,000$, $\lambda_c = \delta$, (*d*) $Re_\theta = 13\,000$, $\lambda_c = 2\delta$.

with the Reynolds number if large enough a cut-off wavelength is used, but slightly decreases if the cut-off $\lambda_c = \delta$ is used. This can easily be explained by the lack of scale separation at the lower Reynolds number that has been previously emphasized. It may be concluded that the large-scale structures seem to contribute to about half of the mean skin friction in the range of Reynolds numbers considered, and that this share may even increase at higher Reynolds numbers. Indeed, as already mentioned for the streamwise velocity fluctuations, the spectra (or co-spectra) give much more reliable information than such integrated values, as a consequence of the lack of scale separation at the considered Reynolds numbers. It should also be remembered that the way the advection velocity is determined in the use of Taylor's hypothesis tends to underestimate the contribution of the larger scales near the wall, as already explained above, which means that their actual contribution to mean wall shear stress may be even higher than estimated here.

Equation (5.15) may be integrated over the wall distance in order to assess the overall contribution of a specified band of wavelengths to $C_{f,2}$. This leads to the definition of a kind of power spectral density of $C_{f,2}$ depending on the wavelength of the contributing structures across the boundary layer, defined as Φ_{C_f}:

$$k_x \Phi_{C_f} = \int_0^1 k_x \Phi_{F_R} \, \mathrm{d}\left(\frac{y}{\delta}\right), \tag{5.16}$$

$$C_{f,2} = \int_{-\infty}^{\infty} k_x \Phi_{C_f} \, \mathrm{d}(\ln(k_x)). \tag{5.17}$$

It should be noted that this quantity does not result from the post-processing of the temporal signal $C_f(t)$ at the wall, which would lead to a different spectrum and have quite a different physical meaning. This is only an indirect way of evaluating the contribution of the wavelengths to $C_{f,2}$ according to the FIK identity, hence to the mean friction coefficient and not its fluctuations. The relative contribution is

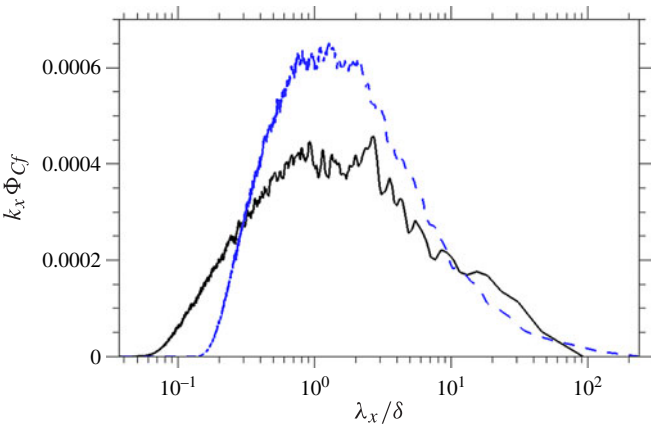

FIGURE 19. (Colour online) Contribution $k_x\Phi_{C_f}$ (5.16) of the physical length scales to $C_{f,2}$: – – –, $Re_\theta = 5200$; ——, $Re_\theta = 13\,000$

directly proportional to the area under the curve of $k_x\Phi_{C_f}$ plotted as a function of the wavelength in logarithmic scales. The results at both Reynolds numbers considered are shown in figure 19.

The overall level of $k_x\Phi_{C_f}$ is lower at the higher Reynolds number because the overall friction coefficient is smaller. The relative contribution of the largest structures slightly increases with the Reynolds number. The maximum of the local contribution in wavelength stays close to δ to 2δ, confirming that the most significant contribution to mean wall shear stress scales in outer units. It may also be noted that the smaller-wavelength part of the spectrum is much broader at the higher Reynolds number. This corresponds to the scale separation that appears in between the two Reynolds numbers: the inner scales become much smaller when non-dimensionalized by the outer scaling for increasing Reynolds numbers. As explained in § 4, assessing the contribution to $C_{f,2}$ actually provides a good insight into the contribution to the overall turbulent extra C_f compared to the laminar C_f, which is shown by (4.20). Figure 19 confirms how significant the contribution of the large scales to mean wall shear stress is at the considered Reynolds numbers and suggests it might become even more significant at higher Reynolds numbers.

6. Conclusion

A simulation of a flat-plate turbulent boundary layer with zero pressure gradient developing over a wide range of Reynolds numbers $3060 \leqslant Re_\theta \leqslant 13\,650$ was performed using the zonal detached eddy simulation (ZDES) technique. The study mainly focused on mean wall shear stress generated by the turbulent boundary layer and especially by the largest-scale coherent structures, a topic that has received surprisingly little attention in the literature in the case of flat-plate boundary layers, compared to channel flows and friction fluctuations.

The simulation is validated at several levels. First of all, the global quantities describing the boundary layer development, such as the mean skin friction coefficient, the shape parameter and Coles' wake factor compare very favourably to the experimental data, and the asymptotic trend towards high Reynolds numbers is well recovered. Simple fits from the literature are compared and adjusted to the available

data, enabling an easier prediction of global quantities at high Reynolds numbers. For instance, a relation between Re_θ and Re_τ is given. Moreover, the comparison of the second-order statistical moments demonstrates the very good resolution of the outer layer. Finally, a more thorough comparison with the experiments is made through the computation of streamwise spectra of the streamwise velocity component.

The energy sites in these spectra reveal the presence of very large-scale motions which are visualized by more direct means. Consistently with previous findings in the literature, e.g. Hutchins & Marusic (2007), these superstructures are found to be approximately 5δ to 6δ long and are meandering with a lateral amplitude of 0.3δ. They have a clear footprint in the inner layer. In addition, hairpins are seen to cluster in what looks like the so-called hairpin packets. The mean inclination angle of the resulting structures is close to 19°, larger than usually reported from experiments, in which it is assessed somewhat differently. However, towards the higher Reynolds numbers considered, the wider range of active scales makes the structures much more complicated, thus making the recognition of hairpins harder. As described in the literature, e.g. in Jiménez *et al.* (2010), the hairpin finally only describes a mean statistical structure made up of many different realizations resulting from smaller-scale structures.

The issue of mean wall shear stress generation according to the wavelength of the turbulent fluctuations is then looked at from the point of view offered by the FIK identity (Fukagata *et al.* 2002). According to this identity, the mean skin friction coefficient results from the weighted integral of the Reynolds shear stress. This identity is widely applied to channel flows, but not as often to the case of a flat-plate boundary layer. Indeed, one major issue that is raised when applying the FIK identity to the flat-plate boundary layer is the presence of a contributing term to C_f which is traditionally seen as describing the spatial heterogeneity of the boundary layer and which vanishes in the case of a channel flow. A new point of view is given here, according to which this term describes the total shear stress variations across the boundary layer, and the behaviour of this term is shown to follow some remarkable self-similarity trends towards high Reynolds numbers. This casts a new light on the traditional use of the FIK identity, giving much support to the common study of the mean skin friction coefficient focusing only on the contributing term related to the Reynolds shear stress, denoted $C_{f,2}$ here.

The integrand F_R of the integral giving $C_{f,2}$ is studied both with respect to the distance to the wall and with respect to the wavelength of the turbulent fluctuations. For the first time to the authors' knowledge, a spectral mapping of F_R is given in the case of the flat-plate turbulent boundary layer. This directly maps the contribution of a given wavelength at a given height to the global friction coefficient. Thanks to this mapping, the contribution of the larger-scale structures to mean friction is assessed. In the considered Reynolds number range, the structures with a streamwise wavelength $\lambda_x > \delta$ contribute to more than 60 % of $C_{f,2}$, and those larger than $\lambda_x > 2\delta$ still represent approximately 45 % of $C_{f,2}$. It is recalled that $C_{f,2}$ amounts to more than 80 % of the overall C_f, which shows how significant the contribution of the very large-scale motions to mean wall shear stress is.

Nevertheless, the very nature of the FIK identity should be kept in mind. Indeed, this identity results from a mathematical transform of the equations rather than from a physical reasoning. This implies that the description of the contributions of given structures at given heights in the boundary layer through the integral giving $C_{f,2}$ cannot lead to conclusions as to causal relations, for instance concerning the interaction between the inner and the outer layer. Even though the present

study demonstrates how significantly the larger structures located in the outer layer contribute to the mean skin friction, and especially suggests that the superstructures may carry a significant contribution to the Reynolds shear stress, it should not be concluded that the structures located in the inner layer play a negligible role in friction generation. The simplest demonstration of this is given by the case of the fully turbulent rough-flat-plate boundary layer, in which the skin friction is much different from the smooth wall case, even though the influence of the surface roughness is expected to impact mainly on the inner layer very close to the wall. Consequently, the study of the interaction between the inner and the outer layer, which has already been widely dealt with in the literature, for instance in Mathis *et al.* (2013) and in Ganapathisubramani *et al.* (2012), but which still raises unanswered questions, will be a natural continuation of the present work. Simulating even higher-Reynolds-number turbulent boundary layers would also prove extremely useful, as the present range of Reynolds numbers has been shown to be hardly sufficient for scale separation and high-Reynolds-number asymptotic trends to arise.

Acknowledgements

This work was performed using HPC resources from GENCI-CINES (Project ZDESWALLTURB, grant 2012-[c2012026817]) to whom the authors are greatly indebted. The authors wish also to thank all the people involved in the past and present evolution of the FLU3M code. Pierre Sagaut and Guillaume Cressent are warmly acknowledged for very stimulating discussions. The thesis of Nicolas Renard is partly funded by the French defence procurement agency DGA.

REFERENCES

ADRIAN, R. J., MEINHART, C. D. & TOMKINS, C. D. 2000 Vortex organization in the outer region of the turbulent boundary layer. *J. Fluid Mech.* **422**, 1–54.

DEL ÁLAMO, J. C. & JIMÉNEZ, J. 2009 Estimation of turbulent convection velocities and corrections to Taylor's approximation. *J. Fluid Mech.* **640**, 5–26.

DEL ÁLAMO, J. C., JIMÉNEZ, J., ZANDONADE, P. & MOSER, R. D. 2004 Scaling of the energy spectra of turbulent channels. *J. Fluid Mech.* **500**, 135–144.

ARAYA, G., CASTILLO, L., MENEVEAU, C. & JANSEN, K. 2011 A dynamic multi-scale approach for turbulent inflow boundary conditions in spatially developing flows. *J. Fluid Mech.* **670**, 581–605.

BALAKUMAR, B. J. & ADRIAN, R. J. 2007 Large- and very-large-scale motions in channel and boundary-layer flows. *Phil. Trans. R. Soc. Lond.* A **365**, 665–681.

BERNARDINI, M. & PIROZZOLI, S. 2011 Inner/outer layer interactions in turbulent boundary layers: A refined measure for the large-scale amplitude modulation mechanism. *Phys. Fluids* **23**, 061701.

CARLIER, J. & STANISLAS, M. 2005 Experimental study of eddy structures in a turbulent boundary layer using particle image velocimetry. *J. Fluid Mech.* **535**, 143–188.

CHOI, H. & MOIN, P. 1994 Compact finite difference schemes with spectral-like resolution. *J. Comput. Phys.* **113** (1), 227–234.

COLES, D. E. 1956 The law of the wake in the turbulent boundary layer. *J. Fluid Mech.* **1**, 191–226.

DANDOIS, J., GARNIER, E. & SAGAUT, P. 2007 Numerical simulation of active separation control by a synthetic jet. *J. Fluid Mech.* **574**, 25–58.

DECK, S. 2005*a* Numerical simulation of transonic buffet over a supercritical airfoil. *AIAA J.* **43** (7), 1556–1566.

DECK, S. 2005*b* Zonal-detached eddy simulation of the flow around a high-lift configuration. *AIAA J.* **43** (11), 2372–2384.

DECK, S. 2012 Recent improvements of the Zonal Detached Eddy Simulation (ZDES) formulation. *Theor. Comput. Fluid Dyn.* **26** (6), 523–550.

DECK, S., DUVEAU, PH., D'ESPINEY, P. & GUILLEN, PH. 2002 Development and application of Spalart Allmaras one equation turbulence model to three-dimensional supersonic complex configurations. *Aerosp. Sci. Technol.* **6** (3), 171–183.

DECK, S. & LARAUFIE, R. 2013 Numerical investigation of the flow dynamics past a three-element aerofoil. *J. Fluid Mech.* **723**, 401–444.

DECK, S. & THORIGNY, P. 2007 Unsteadiness of an axisymmetric separating-reattaching flow: Numerical investigation. *Phys. Fluids* **19**, 065103.

DECK, S., WEISS, P. E., PAMIÈS, M. & GARNIER, E. 2011 Zonal detached eddy simulation of a spatially developing flat plate turbulent boundary layer. *Comput. Fluids* **48**, 1–15.

DEGRAAFF, D. B. & EATON, J. K. 2000 Reynolds number scaling of the flat-plate turbulent boundary layer. *J. Fluid Mech.* **422**, 319–346.

DENNIS, D. J. C. & NICKELS, T. B. 2008 On the limitations of Taylor's hypothesis in constructing long structures in a turbulent boundary layer. *J. Fluid Mech.* **614**, 197–206.

ERM, L. P. & JOUBERT, P. N. 1991 Low-Reynolds-number turbulent boundary layers. *J. Fluid Mech.* **230**, 1–44.

FERNHOLZ, H. H. & FINLEY, P. J. 1996 The incompressible zero-pressure-gradient turbulent boundary layer: an assessment of the data. *Prog. Aerosp. Sci.* **32**, 245–311.

FERRANTE, A. & ELGHOBASHI, S. E. 2009 Reynolds number effect on drag reduction in a microbubble-laden spatially developing boundary layer. *J. Fluid Mech.* **543**, 93–106.

FUKAGATA, K., IWAMOTO, K. & KASAGI, N. 2002 Contribution of Reynolds stress distribution to the skin friction in wall-bounded flows. *Phys. Fluids* **14**, 73–76.

GANAPATHISUBRAMANI, B., CLEMENS, N. T. & DOLLING, D. S. 2006 Large-scale motions in a supersonic turbulent boundary layer. *J. Fluid Mech.* **556**, 271–282.

GANAPATHISUBRAMANI, B., HUTCHINS, N., MONTY, J. P., CHUNG, D. & MARUSIC, I. 2012 Amplitude and frequency modulation in wall turbulence. *J. Fluid Mech.* **712**, 61–91.

GANAPATHISUBRAMANI, B., LONGMIRE, E. K. & MARUSIC, I. 2003 Characteristics of vortex packets in turbulent boundary layers. *J. Fluid Mech.* **478**, 35–46.

GAND, F., DECK, S., BRUNET, V. & SAGAUT, P. 2010 Dynamics over a simplified junction flow. *Phys. Fluids* **22**, 115111.

GOMEZ, T., FLUTET, V. & SAGAUT, P. 1981 Contribution of Reynolds stress distribution to the skin friction in compressible turbulent channel flows. *Phys. Rev.* E **79**, 035301–1/4.

HEAD, M. R. & BANDYOPADHYAY, P. 1981 New aspects of turbulent boundary layer structure. *J. Fluid Mech.* **107**, 297–338.

HOYAS, S. & JIMENEZ, J. 2006 Scaling of velocity fluctuations in turbulent channels up to $Re_\tau = 2003$. *Phys. Fluids* **18**, 011702.

HUDGINS, L., FRIEHE, C. A. & MAYER, M. E. 1993 Wavelet transforms and atmospheric turbulence. *Phys. Rev. Lett.* **71** (20), 3279–3282.

HULTMARK, M., VALLIKIVI, M., BAILEY, S. C. C. & SMITS, A. J. 2013 Logarithmic scaling of turbulence in smooth- and rough-wall pipe flow. *J. Fluid Mech.* **728**, 376–395.

HUTCHINS, N., CHAUHAN, K., MARUSIC, I., MONTY, J. & KLEWICKI, J. 2012 Towards reconciling the large-scale structure of turbulent boundary layers in the atmosphere and laboratory. *Boundary-Layer Meteorol.* **145**, 273–306.

HUTCHINS, N. & MARUSIC, I. 2007 Evidence of very long meandering features in the logarithmic region of turbulent boundary layers. *J. Fluid Mech.* **579**, 1–28.

HUTCHINS, N., MONTY, J. P., GANAPATHISUBRAMANI, B., NG, H. C. H. & MARUSIC, I. 2011 Three-dimensional conditional structure of a high-Reynolds-number turbulent boundary layer. *J. Fluid Mech.* **673**, 255–285.

HUTCHINS, N., NICKELS, T. B., MARUSIC, I. & CHONG, M. S. 2009 Hot-wire spatial resolution issues in wall-bounded turbulence. *J. Fluid Mech.* **635**, 103–136.

HWANG, Y. 2013 Near-wall turbulent fluctuations in the absence of wide outer motions. *J. Fluid Mech.* **723**, 264–288.

ISHIHARA, T., GOTOH, T. & KANEDA, Y. 2009 Study of high-Reynolds number isotropic turbulence by direct numerical simulation. *Annu. Rev. Fluid Mech.* **41**, 165–180.

JARRIN, N., BENHAMADOUCHE, S., LAURENCE, D. & PROSSER, R. 2006 A synthetic-eddy-method for generating inflow conditions for large eddy simulation. *Intl J. Heat Fluid Flow* **27**, 585–593.

JIMÉNEZ, J. 1998 The largest scales of turbulent wall flows. *CTR Annu. Res. Briefs* pp. 137–154. Center for Turbulence Research.

JIMÉNEZ, J. 2003 Computing high-Reynolds-number turbulence: will simulations ever replace experiments?. *J. Turbul.* **4** (22), 14.

JIMÉNEZ, J. 2012 Cascades in wall-bounded turbulence. *Annu. Rev. Fluid Mech.* **44**, 27–45.

JIMÉNEZ, J., DEL ÁLAMO, J. C. & FLORES, O. 2004 The large-scale dynamics of near-wall turbulence. *J. Fluid Mech.* **505**, 179–199.

JIMÉNEZ, J., HOYAS, S., SIMENS, M. P. & MIZUNO, Y. 2010 Turbulent boundary layers and channels at moderate Reynolds numbers. *J. Fluid Mech.* **657**, 335–360.

JIMÉNEZ, J. & PINELLI, A. 1999 The autonomous cycle of near-wall turbulence. *J. Fluid Mech.* **389**, 335–359.

KANEDA, Y. & ISHIHARA, T. 2006 High-resolution direct numerical simulation of turbulence. *J. Turbul.* **7** (20), 14.

KANEDA, Y., MORISHITA, K. & ISHIHARA, T. 2013 Small scale universality and spectral characteristics in turbulent flows. In *Symposium on Turbulence and Shear Flow Phenomena (TSFP-8), Poitiers, France.*

KLEWICKI, J. C. 2010 Reynolds number dependence, scaling, and dynamics of turbulent boundary layers. *Trans. ASME: J. Fluids Engng* **132**, 094001.

KROGSTAD, P.-Å., ANTONIA, R. A. & BROWNE, L. W. B. 1992 Comparison between rough- and smooth-wall turbulent boundary layers. *J. Fluid Mech.* **245**, 599–617.

KROGSTAD, P.-Å., KASPERSEN, J. H. & RIMESTAD, S. 1998 Convection velocities in a turbulent boundary layer. *Phys. Fluids* **10** (4), 949–957.

KUNKEL, G. J. & MARUSIC, I. 2006 Study of the near-wall-turbulent region of the high-Reynolds-number boundary layer using an atmospheric flow. *J. Fluid Mech.* **548**, 375–402.

LARAUFIE, R. & DECK, S. 2013 Assessment of Reynolds stresses tensor reconstruction methods for synthetic inflow conditions. Application to hybrid RANS/LES methods. *Intl J. Heat Fluid Flow* **42**, 68–78.

LARAUFIE, R., DECK, S. & SAGAUT, P. 2011 A dynamic forcing method for unsteady turbulent inflow conditions. *J. Comput. Phys.* **230** (23), 8647–8663.

LARAUFIE, R., DECK, S. & SAGAUT, P. 2012 A rapid switch from RANS to WMLES for spatially developing boundary layers. In *Progress in Hybrid RANS-LES Modelling* (ed. S. Fu, W. Haase, S.-H. Peng & D. Schwamborn), vol. 117, pp. 147–156. Springer.

LARCHEVÊQUE, L., SAGAUT, P., LE, T. H. & COMTE, P. 1997 Large-eddy simulation of a compressible flow in a three-dimensional open cavity at high Reynolds number. *J. Fluid Mech.* **516**, 265–301.

LEE, J., JUNG, S. Y., SUNG, H. J. & ZAKI, T. A. 2013 Effect of wall heating on turbulent boundary layers with temperature-dependent viscosity. *J. Fluid Mech.* **726**, 196–225.

LEE, J. H. & SUNG, H. J. 2011 Direct numerical simulation of a turbulent boundary layer up to $Re_\theta = 2500$. *Intl J. Heat Fluid Flow* **32**, 1–10.

LEE, J. H. & SUNG, H. J. 2013 Comparison of very-large-scale motions of turbulent pipe and boundary layer simulations. *Phys. Fluids* **25**, 045103.

MARQUILLIE, M., EHRENSTEIN, U. & LAVAL, J.-P. 2011 Instability of streaks in wall turbulence with adverse pressure gradient. *J. Fluid Mech.* **681**, 205–240.

MARUSIC, I. & HEUER, W. D. C. 2007 Reynolds number invariance of the structure inclination angle in wall turbulence. *Phys. Rev. Lett.* **99**, 114504.

MARUSIC, I. & HUTCHINS, N. 2005 Experimental study of wall turbulence: implications for control. In *Transition And Turbulence Control* (ed. M. Gad-el-Hak & H. M. Tsai), Lecture Notes Series, Institute for Mathematical Sciences, National University of Singapore, vol. 8, pp. 1–40.

MARUSIC, I. & KUNKEL, G. J. 2003 Streamwise turbulence intensity formulation for flat-plate boundary layers. *Phys. Fluids* **15**, 2461–2464.

MARUSIC, I., LI, J. D. & PERRY, A. E. 1989 A study of the Reynolds-shear-stress spectra in zero-pressure-gradient boundary layers. In *Tenth Australian Fluid Mechanics Conference – University of Melbourne.*

MARUSIC, I., MATHIS, R. & HUTCHINS, N. 2010*a* High Reynolds number effects in wall turbulence. *Intl J. Heat Fluid Flow* **31**, 418–428.

MARUSIC, I., MATHIS, R. & HUTCHINS, N. 2010*b* Predictive model for wall-bounded turbulent flow. *Science* **329**, 193–196.

MARUSIC, I., MCKEON, B. J., MONKEWITZ, P. A., NAGIB, H. M., SMITS, A. J. & SREENIVASAN, K. R. 2010 Wall-bounded turbulent flows at high Reynolds numbers: Recent advances and key issues. *Phys. Fluids* **22**, 065103.

MARUSIC, I., MONTY, J. P., HULTMARK, M. & SMITS, A. J. 2012 On the logarithmic region in wall turbulence. *J. Fluid Mech.* **716**, 1–11.

MARUSIC, I., UDDIN, A. K. M. & PERRY, A. E. 1997 Similarity law for the streamwise turbulence intensity in zero-pressure-gradient turbulent boundary layers. *Phys. Fluids* **9**, 3718–3726.

MARY, I. & SAGAUT, P. 2002 Large eddy simulation of flow around an airfoil near stall. *AIAA J.* **40** (6), 1139–1145.

MATHIS, R., HUTCHINS, N. & MARUSIC, I. 2009 Large-scale amplitude modulation of the small-scale structures in turbulent boundary layers. *J. Fluid Mech.* **628**, 311–337.

MATHIS, R., MARUSIC, I., CHERNYSHENKO, S. I. & HUTCHINS, N. 2013 Estimating wall-shear-stress fluctuations given an outer region input. *J. Fluid Mech.* **715**, 163–180.

MATHIS, R., MARUSIC, I., HUTCHINS, N. & SREENIVASAN, K. R. 2011 The relationship between the velocity skewness and the amplitude modulation of the small scale by the large scale in turbulent boundary layers. *Phys. Fluids* **23**, 121702.

MICHEL, R., QUÉMARD, C. & DURANT, R. 1969 Application d'un schéma de longueur de mélange à l'étude des couches limites turbulentes d'équilibre. *ONERA Note Tech.* 154.

NAGIB, H. M., CHAUHAN, K. A. & MONKEWITZ, P. A. 2007 Approach to an asymptotic state for zero pressure gradient turbulent boundary layer. *Phil. Trans. R. Soc. Lond.* A **365**, 755–770.

NAGIB, H. M., CHRISTOPHOROU, C., REUDI, J.-D., MONKEWITZ, P. A., ÖSTERLUND, J. & GRAVANTE, S. 2004 Can we ever rely on results from wall-bounded turbulent flows without direct measurements of wall shear stress?. In *24th AIAA Aerodynamic Measurement Technology and Ground Testing Conference.*

NICKELS, T. B. & MARUSIC, I. 2001 On the different contributions of coherent structures to the spectra of a turbulent round jet and a turbulent boundary layer. *J. Fluid Mech.* **448**, 367–385.

ÖSTERLUND, J. M., JOHANSSON, A. V., NAGIB, H. M. & HITES, M. 2000 A note on the overlap region in turbulent boundary layers. *Phys. Fluids* **12**, 1–4.

PAMIÈS, M., WEISS, P. E., DECK, S. & SAGAUT, P. 2009 Generation of synthetic turbulent inflow data for large eddy simulation of spatially evolving wall-bounded flows. *Phys. Fluids* **21**, 045103.

PANTON, R. L. 2001 Overview of the self-sustaining mechanisms of wall turbulence. *Prog. Aerosp. Sci.* **37**, 341–383.

PÉCHIER, T. V., GUILLEN, L. G. & CAYSAC, M. A. 2001 Magnus effect over finned projectiles. *AIAA J. Spacecr. Rockets* **38** (4), 542–549.

PEET, Y. & SAGAUT, P. 2009 Theoretical prediction of skin friction on geometrically complex surface. *Phys. Fluids* **21**, 105105.

PERRY, A. E. & MARUSIC, I. 1995 A wake model for the turbulence structure of boundary layers. Part 1. Extension of the attached eddy hypothesis. *J. Fluid Mech.* **298**, 361–388.

PERRY, A. E., MARUSIC, I. & JONES, M. B. 2002 On the streamwise evolution of turbulent boundary layers in arbitrary pressure gradients. *J. Fluid Mech.* **461**, 61–91.

PIROZZOLI, S. & BERNARDINI, M. 2013 Probing high-Reynolds number effects in numerical boundary layers. *Phys. Fluids* **25**, 021704.

PRIYADARSHANA, P. J. A. & KLEWICKI, J. C. 2004 Study of the motions contributing to the Reynolds stress in high and low Reynolds number turbulent boundary layers. *Phys. Fluids* **16**, 4586–4600.

ROBINSON, S. K. 1991 Coherent motions in the turbulent boundary layer. *Annu. Rev. Fluid Mech.* **23**, 601–639.

SADDOUGHI, S. G. & VEERAVALLI, S. V. 1994 Local isotropy in turbulent boundary layers at high Reynolds number. *J. Fluid Mech.* **268**, 333–372.

SAGAUT, P. & DECK, S. 2009 Large eddy simulation for aerodynamics: Status and perspectives. *Phil. Trans. R. Soc. Lond.* A **367**, 2849–2860.

SAGAUT, P., DECK, S. & TERRACOL, M. 2013 *Multiscale and Multiresolution Approaches in Turbulence: A Comprehensive Introduction to Modern LES, DES and Hybrid RANS/LES Methods with Examples*. 2nd Edn. Imperial College Press.

SCHLATTER, P., LI, Q., BRETHOUWER, G., JOHANSSON, A. & HENNINGSON, D. 2010 Simulations of spatially evolving turbulent boundary layers up to $Re_\theta = 4300$. *Intl J. Heat Fluid Flow* **31**, 251–261.

SCHLATTER, P. & ÖRLÜ, R. 2010*a* Assessment of direct simulation data of turbulent boundary layers. *J. Fluid Mech.* **659**, 116–126.

SCHLATTER, P. & ÖRLÜ, R. 2010*b* Quantifying the interaction between large and small scales in wall-bounded turbulent flows: A note of caution. *Phys. Fluids* **22**, 051704.

SCHLICHTING, H. 1968 *Boundary-Layer Theory*. McGraw-Hill.

SILLERO, J., JIMENEZ, J., MOSER, R. D. & MALAYA, N. P. 2011 Direct simulation of a zero-pressure-gradient turbulent boundary layer up to $Re_\theta = 6650$. In *13th European Turbulence Conference (ETC13), J. Phys.: Conf. Series* 318, 022023. IOP.

SIMENS, M. P., JIMÉNEZ, J., HOYAS, S. & MIZUNO, Y. 2009 A high-resolution code for turbulent boundary layers. *J. Comput. Phys.* **228**, 4218–4231.

SIMON, F., DECK, S., GUILLEN, PH., SAGAUT, P. & MERLEN, A. 2007 Numerical simulation of the compressible mixing layer past an axisymmetric trailing edge. *J. Fluid Mech.* **591**, 215–253.

SMITH, R. W. 1994 Effect of Reynolds number on the structure of turbulent boundary layers. PhD thesis, Department of Mechanical and Aerospace Engineering, Princeton University.

SMITS, A. J., MCKEON, B. J. & MARUSIC, I. 2011 High Reynolds number wall turbulence. *Annu. Rev. Fluid Mech.* **43** (1), 353–375.

SPALART, P. R. 1988 Direct simulation of a turbulent boundary layer up to $Re_\theta = 1400$. *J. Fluid Mech.* **187**, 61–98.

SPALART, P. R. & ALLMARAS, S. R. 1992 A one equation turbulence model for aerodynamic flows. *AIAA Paper* 92-0439.

TOWNSEND, A. A. 1976 *The Structure of Turbulent Shear Flow*. Cambridge University Press.

TROMEUR, E., GARNIER, E. & SAGAUT, P. 2006 ES of aero-optical effects in turbulent boundary layer. *J. Turbul.* **7** (1), 28.

WEISS, P. E. & DECK, S. 2011 Control of the antisymmetric mode ($m = 1$) for high Reynolds axisymmetric separating/reattaching flows. *Phys. Fluids* **23**, 095102.

WEISS, P. E., DECK, S., ROBINET, J. C. & SAGAUT, P. 2009 On the dynamics of axisymmetric turbulent separating/reattaching flows. *Phys. Fluids* **21**, 075103.

WU, X. & MOIN, P. 2009 Direct numerical simulation of turbulence in a nominally zero-pressure gradient flat-plate boundary layer. *J. Fluid Mech.* **630**, 5–41.